ACS OMEGA

Open Access

http://pubs.acs.org/journal/acsodf

Review

Review of Transition Metal Chalcogenides and Halides as Electrode Materials for Thermal Batteries and Secondary Energy Storage Systems

Premnath Muthu,* Sudha Rajagopal, Devishree Saju, Vidyashri Kesavan, Arun Dellus, Loganathan Sadhasivam,* and Naveen Chandrasekaran*

Cite This: *ACS Omega* 2024, 9, 7357−7374

Read Online

ACCESS | Metrics & More | Article Recommendations

ABSTRACT: Transition metal chalcogenides and halides (TMCs and TMHs) have been extensively used and reported as electrode materials in diverse primary and secondary batteries. This review summarizes the suitability of TMCs and TMHs as electrode materials focusing on thermal batteries (utilized for defense applications) and energy storage systems like mono- and multivalent rechargeable batteries. The report also identifies the specific physicochemical properties that need to be achieved for the same materials to be employed as cathode materials in thermal batteries and anode materials in monovalent rechargeable systems. For example, thermal stability of the materials plays a crucial role in delivering the performance of the thermal battery system, whereas the electrical conductivity and layered structure of similar materials play a vital role in enhancing the electrochemical performance of the mono- and multivalent rechargeable batteries. It can be summarized that nonlayered CoS_2, FeS_2, NiS_2, and WS_2 were found to be ideal as cathode materials for thermal batteries primarily due to their better thermal stability, whereas the layered structures of these materials with a coating of carbon allotrope (CNT, graphene, rGO) were found to be suitable as anode materials for monovalent alkali metal ion rechargeable batteries. On the other hand, vanadium, titanium, molybdenum, tin, and antimony based chalcogenides were found to be suitable as cathode materials for multivalent rechargeable batteries due to the high oxidation state of cathode materials which resists the stronger field produced during the interaction of di- and trivalent ions with the cathode material facilitating higher energy density with minimal structural and volume changes at a high rate of discharge.

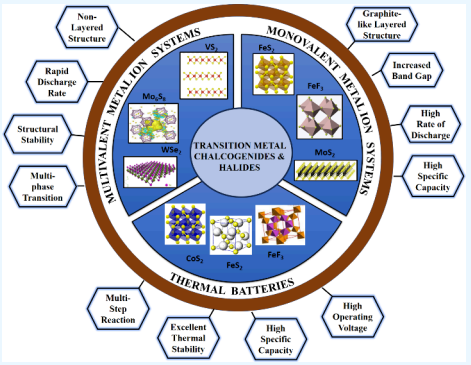

1. INTRODUCTION

Metal chalcogenides and halides are multivalent materials in the field of energy storage and conversion, which have gained significant attention due to their potential to deliver high specific capacity, approaching theoretical limits, owing to their semiconducting nature and appropriate energy bandgaps.[1] Transition metal chalcogenides (TMCs) exist in the form of either metal tellurides, selenides, or sulfides (metal cation, M = Co, Fe, Ni, Mn, V, Ti, Zn, Mo, W and chalcogen anion, X = Te, Se, S) and can be classified as layered and nonlayered metal chalcogenides.[2,3] TMCs are promising materials for rechargeable batteries, particularly due to their ability to facilitate fast intercalation and deintercalation of both monovalent and multivalent ions. Figure 1 depicts the recent advances and historical development in the electrode materials of thermal batteries. This property is crucial for enhancing the charging and discharging rates of batteries, leading to improved overall performance and efficiency. These materials typically have an open structure with weak interactive van der Waals forces between individual layers, allowing for efficient ion diffusion within the material. However, due to strong covalent

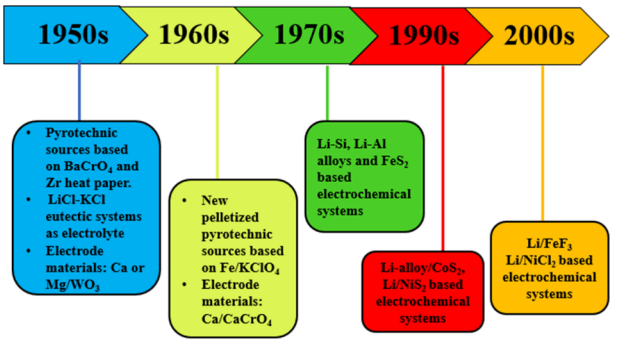

Figure 1. Historical development in the electrode materials of thermal batteries.

Received: November 6, 2023
Revised: January 9, 2024
Accepted: January 19, 2024
Published: February 9, 2024

bonds, atoms are bound with X-M-X layers and form a graphene-like sandwich structure which can play a crucial role in their stability and suitability as host materials for a variety of ions (Li, Na, K, Mg, Zn, Al) in rechargeable batteries.[4−6] Solid-state diffusion kinetics is the foremost existing problem in TMCs cathode materials making the kinetics sluggish. A few approaches that can be used to overcome the ion transport kinetic constraints associated with solid-state diffusion in TMCs cathode materials are (1) the band gap energy effect: Formation of a heterojunction alters the band gap energy at the interface of different materials which induces an electron flux and creates a stronger electric field at the heterointerface during the electrochemical cycle. This enhanced electric field promotes excellent ionic diffusion kinetics by facilitating faster movement of ions within the material. (2) Lattice vacancy effect: Lattice vacancies, such as S atom, F atom, or Se-atom vacancies, are intentionally created during the synthesis of heterostructured metal chalcogenides. These halide or chalcogenide interstitial atoms vacancies act as effective negative charge centers, attracting alkali metal ions and inducing excess electrons, thus promoting ionic diffusion kinetics. Lattice vacancies act as electronic charge carriers, enhancing Coulombic efficiency by providing additional active sites for redox reactions. (3) Synergistic effect: Metal chalcogenides possess a high adsorption ability toward poly sulfides, -fluorides, and selenides. It can facilitate the conversion of polyhalides, acting as catalytic agents in various electrochemical reactions. Metal chalcogenides with hetero-structures create rich active interfaces, enabling efficient trapping and conversion of polyhalides, thus enhancing the overall battery performance.[7,8]

In the current context, lithium-ion batteries (LIBs) are considered the predominant and benchmarked candidates among various battery technologies which have made them the preferred choice for a wide range of applications, contributing to their dominance in the battery market especially in the context of portable electronics, electric vehicles, and grid energy storage.[9] The key advantages of LIBs that contribute to their widespread use and recognition include high operating voltage, high reversible capacity, high energy density, high mechanical stability, and high efficiency. Rechargeable batteries have seen significant research focus, particularly in the development of electrode materials, across various types. The four major types that represent different classes of rechargeable batteries, each with its unique characteristics and research priorities are as follows: (a) Alkali metal-ion batteries, viz., Li-ion, Na-ion, and K-ion, (b) multivalent metal-ion batteries viz., Mg-ion, Al-ion, and Zn-ion, (c) Li-S battery, and (d) metal-air batteries.[10,11] Under the metal-air rechargeable type series, there are two categories namely (a) electrically rechargeable batteries and (b) mechanically rechargeable metal-air batteries, which are neither electrically rechargeable nor primary type such as Li-air, Mg-air, Al-air, and Zn-air.[8] In the realm of primary (nonrechargeable) batteries, each with its own specific characteristics and applications, there are several batteries which include the following: alkaline batteries (Zn-carbon, Zn-AgO, Zn-MnO_2, Zn-HgO, Cd-HgO), sea water batteries (Mg-AgCl, Mg-CuCl, Al-AgCl) and Li-MX_2/ MX_3 (Li-FeS_2, Li-CoS_2, Li-FeF_3, Li-CuF_3) based molten salt thermal batteries, and a few other primary batteries which include Li-MnO_2, and Mg-MnO_2.[11] The choice of primary battery chemistry depends on the specific requirements of the application. Factors such as energy density, shelf life, environmental considerations, and cost play a role in selecting the most appropriate battery type. Some primary batteries, like alkaline batteries, are widely available and used for everyday devices, while others, like seawater batteries and molten salt thermal batteries, have more specialized strategic applications.[12]

One of the examples is thermal batteries, which are a unique class of high-temperature reserve primary batteries known for their reliability and long-shelf life. These are categorized into different generations based on their chemistry and functional properties. The first-generation thermal batteries (Ca/$CaCrO_4$-based batteries) were initially developed in the 1940s. These batteries typically consist of a calcium anode and a cathode material containing calcium chromate ($CaCrO_4$) and iron disulfide (FeS_2) and are known for their ability to provide high-energy output over a relatively short duration, making them suitable for applications where a burst of power is required.[13] The second generation of thermal batteries is exemplified by lithium/sulfides-based systems, which serve as an alternative to first-generation Ca/$CaCrO_4$-based batteries.[14] These batteries have become prevalent in military applications due to several attractive features like fast activation, large discharge plateau with power and time, long shelf lives, easy installation, and high thermal stability.[15] Second-generation thermal batteries, such as Li/FeS_2 batteries, are used to power various military devices, including actuators for guided weapons, torpedoes, nuclear weapons, and space vehicle weapons.[16] The choice of thermal battery based on the generation and chemistry depends on the specific requirements of the application, including the need for high-temperature operation, long shelf life, and reliable power output. The second-generation lithium/sulfides-based thermal batteries, like Li/FeS_2, have gained popularity in military and aerospace applications due to their superior properties and versatility. However, the Li-Si/LiCl-KCl/FeS_2 thermal battery fails to fulfill certain requirements, and new developments on thermal battery are significantly required to fulfill the overall needs.[17] As technology and operational demands continue to evolve, ongoing research and development in thermal battery technology are crucial to meet the ever-changing needs of various industries, including military and aerospace. In general, thermal batteries consist of three main components, which are cathode (transition metal (TM) sulfides/fluorides/metal chloride/oxides), separator, molten salt electrolyte (LiCl-KCl), anode (Li(Si)/ LiAl/LiB alloy), and a pyrotechnic ignition source.[18] During the missile's operation, the thermal battery is activated by the stimulation of a molten salt electrolyte using exhaust/waste heat generated from the missile. During the indolent state, the battery can be stockpiled for more than 10 years of lifetime, and during the energy requirement, it can be thermally activated at high temperatures of about 350−550 °C using a pyrotechnic source included within the battery.[19] The two distinct pyrotechnic sources which are used include a fuse strip (i.e., "heat paper"), which is made with a blend of Zr/$BaCrO_4$ material, and another source is a "heat" pellet, which is made with a blend of Fe/$KClO_4$. Through direct contact, the heat pellet (Zr/$BaCrO_4$) ignites each of the "heat paper", and after which it proceeds with the thermal activation (100s milliseconds for larger power batteries and 40 ms for small pulse batteries are the time ranges required for thermal activation). KCl-LiCl eutectic mixture is employed as a desirable electrolyte in thermal batteries due to its high ionic conductivity (1.85 S cm^{-1} at 500 °C). However, the drawback of the above system lies in the formation of dendrite-

https://doi.org/10.1021/acsomega.3c08809
ACS Omega 2024, 9, 7357−7374

like structure (upon melting) on the electrode material leading to low open circuit voltage and low operating energy density, resulting in poor electrochemical performances.[20,21] Hence a highly compatible system with electrode and electrolyte countering these drawbacks needs to be designed and developed.

Owing to their fascinating physicochemical and electrochemical properties and due to the ease in modification of their structure, metal-chalcogenides (TMCs) and halides (TMHs) are versatile materials that find applications in various energy storage systems, including both thermal batteries and rechargeable metal-ion batteries. These materials have the potential to serve as cathode materials in thermal batteries and as electrocatalysts in rechargeable metal-ion batteries.[22] For a material to be qualified as an ideal negative electrode, the material is expected to possess high operating potential and multivoltage plateaus and should undergo multiphase formation and prevent oxidation during its discharge in the case of monovalent ion batteries. (Figure 2 shows the variations in

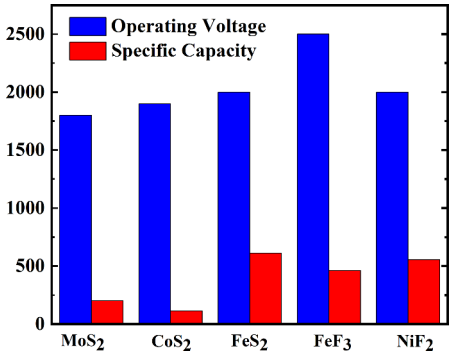

Figure 2. Graph displaying the variations in the operating voltage and specific capacity for different metal chalcogenides and halide-based electrode materials.

operating voltage and specific capacity associated different electrode materials for rechargeable/nonrechargeable metal ion batteries). On the other hand, when employed as positive electrode in thermal batteries, the material is expected to possess (1) high thermal decomposition temperature in addition to the reduction in ohmic polarization resistance, (2) less emission of halogen gases accompanied by inevitable chemical reactions, (3) minimized self-discharge reactions to reduce the solubility rate of cathode materials in molten electrolytes, and (4) inert toward moisture or oxygen.[23]

The above-mentioned characteristics have prompted researchers to continuously explore new materials to meet the specific demands of these applications and create materials that provide efficient and reliable energy storage and electrocatalytic capabilities, contributing to advancements in battery technology for various purposes, from military to renewable energy storage. Among the Li free electrode materials, metal chalcogenides and halides have become potential electrocatalysts, especially in secondary batteries, such as LIB and NIB and considered as a replacement for inert carbon materials. Figure 2 depicts the different synthetic strategies adopted for preparation of TMCs and TMHs.

Various synthetic techniques have been employed (Figure 3) for the preparation of TMC and TMHs such as hydrothermal, thermal sulfuration, reflux method, spray pyrolysis, electrochemical deposition, chemical vapor deposition, and mechanical milling.[24] Due to the ease of operation and scalability, hydrothermal and solvothermal techniques are widely employed, and in the context of electrode fabrication, researchers ought to focus on developing a thin cathode fabrication process which involves addressing key factors for surpassing the technical challenges likely high specific capacity (which allows the battery to store more energy) and good electrochemical stability to ensure a long cycle life. To achieve these beneficial properties, the ideal choice of metal salts with the right combination of chalcogenides or halides with proper active material and binder needs to be achieved.

Furthermore, the fabrication of the electrode material also plays a crucial role in attaining the uniform thickness and porosity to facilitate facile electronic and ionic conduction. The most common electrode fabrication processes are tape casting and spray coating which render uniform thickness and porosity to achieve the desired electrochemical performance. The specific surface area (SSA) of the electrode material is another critical factor in the battery performance. High SSA provides a larger contact area between the electrolyte and the active material thereby providing high reversible specific capacity and energy density.[25] This increased contact area promotes electrochemical reactions and enhances the efficiency of the

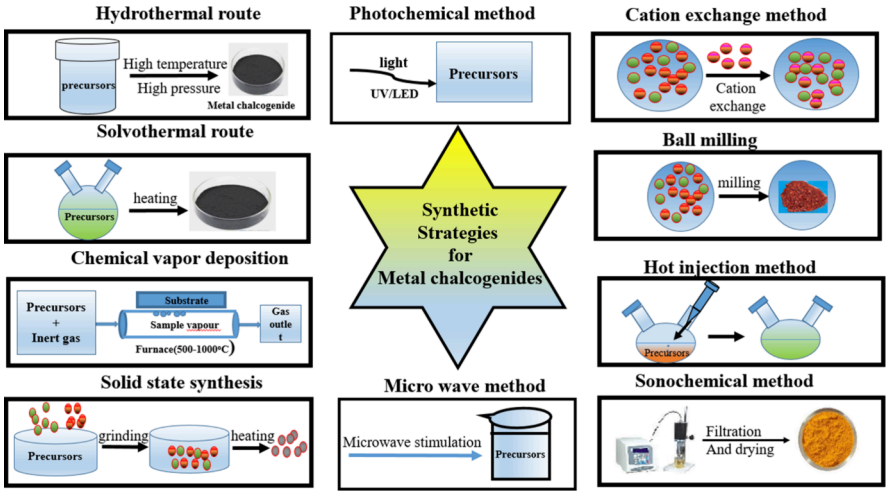

Figure 3. Different synthetic strategies adopted for TMCs and TMHs.

https://doi.org/10.1021/acsomega.3c08809
ACS Omega 2024, 9, 7357−7374

battery, consequently confining the ionic transfer pathways. However, inherently there are few bottlenecked properties, which include huge volume expansion, low electronic conductivity, and thermally unstable structure. Recently, the researchers have undertaken effective strategies to promote structural integrity and cycling stability by incorporating lattice defects (vacancies or dopants) in electrode materials, an open layered structure with expanded spacing (>6 Å), and coalescence of MOFs/rGO with metal chalcogenides, which can provide high conductivity and a specific surface area.[26]

This review summarizes the physicochemical and electrochemical properties and identification of ideal TMCs and TMHs as cathode and anode materials for primary (thermal) and secondary batteries. Figure 4 depicts radar plots charting the performances of TMCs and TMHs.

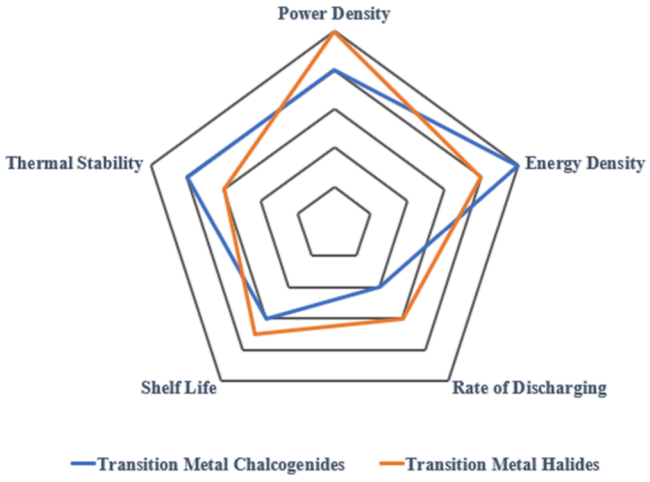

Figure 4. Radar chart comparing the performance parameters of TMCs and TMHs.

2. TMCs AND TMHs AS CATHODE MATERIALS FOR PRIMARY RESERVED THERMAL BATTERIES

Iron disulfide (FeS_2) can be synthesized via the hydrothermal method using $FeSO_4$, $Na_2S_2O_3$, and S as precursors. The synthetic FeS_2 can exist in two crystal structures, namely pyrite (simple-cubic) and marcasite (orthorhombic). (FeS_2), commonly known as pyrite, is a thermally stable material and found to exhibit a relatively high discharge voltage (2.1 V), making it suitable as a cathode material for thermal batteries. Its high theoretical capacity (1206 As g^{-1}), makes it an ideal material to store a significant amount of electrical charge per unit mass, which is crucial for maximizing the energy storage capability of a battery. Being a semiconducting material with an approximate bandgap of 0.95 eV (absorption coefficient > 10^5 cm^{-1}) and a thermal stability of 550 °C helps to maintain its structural integrity and electrochemical properties even at high temperatures, thus making it a suitable choice for electrode materials in high temperature energy storage applications. However, FeS_2 has its own limitations such as the decomposition at a temperature above 550 °C temperature, which can restrict its use in very high-temperature environments. At higher temperatures greater than 550 °C, FeS_2 was found to thermally decompose to pyrrhotite $FeS_{1.14}$ and as sulfur gas (S_2) as given in eq 1.

$$FeS_2 \rightarrow FeS_{1.14} + 0.43S_2 \quad (1)$$

The $FeS_{1.14}$ produced at these temperatures can be separated, if the S_2 gas is perpetually evacuated from FeS_2. Embedding FeS_2 grains in a liquid LiCl-KCl salt and trapping S_2 gas within $FeS_{1.14}$'s porous layer can indeed affect the decomposition behavior of FeS_2. This configuration can act as a barrier to S_2 gas diffusion and influence the overall thermal stability of the system.[27,28]

The thermal decomposition of FeS_2 into $FeS_{1.14}$ and sulfur gas can lead to the formation of a porous structure on the outer surface of FeS_2 grains, which can reduce the structural integrity of the electrode and active centers where new reactions can occur. These new reactions might not be reversible, leading to a capacity fade over time. As the decomposition reaction progresses, the particle size of FeS_2 decreases. Smaller particles tend to have a higher surface area, which can lead to higher reactivity with the electrolyte or other components in the system. This increased reactivity can contribute to capacity fading by causing side reactions and irreversible changes in the electrode material. The presence of molten salts in the system can affect the stability of pyrrhotite ($FeS_{1.14}$). Pyrrhotite may partially dissolve in the molten salts, leading to the loss of active material from the electrode, which can reduce the overall capacity of the cathode over time, contributing to capacity fade. However, if FeS_2 contains contaminants, viz., oxides, sulfates, and elemental sulfur, a high voltage transient ("spike") occurs upon thermal activation. During the discharging process, FeS_2 undergoes three steps of phase transformation, which are segregated into three parts of inversion voltage plateaus as given in eq 2. First step reaction is the Z-phase, which occurs at 1.85 V where the Li reacts with FeS_2 forming $Li_2Fe_2S_4$, the second step reaction is the J-phase, which occurs at 1.65 V where $Li_3Fe_2S_4$ is formed, and the X-phase, the final step, occurs at 1.3 V during which elemental Li, S, and Fe are produced.

$$FeS_2 \rightarrow Li_3Fe_2S_4 \rightarrow Li_{2+x}Fe_{1-x}S_2 \rightarrow Fe \quad (2)$$

Addition of lithium oxide (Li_2O) to the pyrite favors faster reaction kinetics and promotes the formation of $Li_3Fe_2S_4$. Moreover, a small amount (1−2 wt %) of Li_2O/Li_2S (as a lithiation agent) addition overcomes the problem of Fe_2O_3 formation, which is likely to be formed due to the thermal decomposition of sulfides. The pyrite is highly stable and remains unchanged with a minuscule addition of Li_2O material. However, the addition of a higher amount of Li_2O favors the reduction of pyrite's decomposition temperature by ∼100 °C. The sulfides which are unstable get dissolved in the eutectic LiCl-KCl molten salts, and its formation in the eutectic salt can be enhanced with the presence of oxides. Further, the new phase, Li_2FeS_2, is formed due to the reaction between the remaining pyrrhotite and dissolved sulfides as shown in eq 3.

$$FeS + 2Li^+ + S^{2-} \rightarrow Li_2FeS_2 \quad (3)$$

Development of a FeS_2/LiCl-KCl based composite cathode using the plasma spraying method revealed the result of low impedance, i.e., almost 3.5 fold lower than the discrete pressed-powder. The diffusion coefficients of FeS_2 in eutectic LiCl-KCl and without a eutectic mixture are 1.68×10^{-7} cm^2 s^{-1} and 4.21×10^{-8} respectively.[29−31] A FeS_2 thin cathode is developed with an addition of polyimide-*co*-siloxane (PIS) binder using a tape casting technique, and the binder was thermally stable only up to 400 °C and decomposed at 450 °C leading to the disintegration of the cathode material. During thermal decomposition, the organic binder melted and

https://doi.org/10.1021/acsomega.3c08809
ACS Omega 2024, 9, 7357−7374

Table 1. List of Various TMCs and TMHs Employed As Cathode Materials in Thermal Batteries

cathode materials	anode alloy	specific capacity (A g^{-1})	operating voltage (V)	cut-off voltage (V)	discharge temperature (°C)	references
FeS_2	Li-Si	1100−1200	1.9−2.1	1.3	500	42, 43
CoS_2	Li-B/Li-Si	1800/1200	1.8−2.0	1.1	500−520	44, 45
NiS_2	Li-B	1350	1.8−2.0	1.4	500	46
MoS_2	Li-Si	275	1.8	1.2	450	47
WS_2	Li-B	1200	1.4	1.4	500	48
FeF_3	Li-B	290−575	2.5	1.5	500	49
NiF_2	Li-B	900	2.0	0.5	550	50
CuF_2	Li-B	600−1900	3.25	1.5	500	51
$NiCl_2$	Li-B	900	2.0	1.6	500	52

produced gas, resulting in residual materials that created polarization resistance, negatively impacting the electrochemical performance. To address the issue of thermal stability, multiwalled carbon nanotubes (MWCNTs) were introduced as a binder and conductor in the FeS_2 material. This approach aimed to improve both thermal stability and electrochemical performance. The FeS_2-MWCNT composite demonstrated a higher specific capacity and better thermal stability with only a 5% mass reduction rate at 500 °C. Single cells using FeS_2 foam and Fe metal foam as electrodes achieved high discharge capacities of 538 As g^{-1} and 404 As g^{-1}, respectively, at a cutoff voltage of 1.3 V. Notably, when using nanoscale FeS_2 (n-FeS_2) as a cathode material, the cutoff voltage increased to 1.67 V at a current density of 50 mA cm^{-2}, with an average operation time of 1205 s, showing a 20.9% increase in operation time compared to microscale FeS_2 (μ-FeS_2) at the same current density. This indicated that n-FeS_2 had a significant advantage in terms of extended operation time. The trend of high specific capacity and longer operation time was maintained even at higher current densities of 200 mA cm^{-2}, suggesting the potential suitability of n-FeS_2 for high-power applications.[32−34] Although FeS_2 is available in abundance, the lower thermal stability and lower cell voltage and lower specific capacity rendered to the thermal battery system have prompted researchers to look for alternate materials suitable for high temperature power generating systems.

CoS_2 is considered a promising alternative to FeS_2 as a cathode material for specific high-power and long-discharging thermal batteries. It offers several advantages, including flat voltage discharge plateaus at a high nominal voltage (∼1.8 V), a high theoretical capacity (1045 As g^{-1}), high thermal stability (up to 650 °C which is an advantage over FeS_2), high electronic conductivity, poor solubility in eutectic molten salt electrolytes, and low polarization even under high current densities. In general, a Co−S phase diagram includes four distinct phases viz., CoS_2, Co_3S_4, Co_9S_8, and CoS with the space group of $Pa\bar{3}$, $Fd\bar{3}m$, $Fm\bar{3}m$, and $P63/mmc$ respectively, each with its own crystal structure and properties.[35−37] Similar to FeS_2, CoS_2 has a pyrite structure with Co atoms bonded to six sulfur atoms, forming a face-centered array of Co atoms with distorted corner atoms. Co_3S_4 exhibits a spinel structure with two types of Co sites: tetrahedral and octahedral, both coordinated by sulfur atoms. Co_9S_8 has two sites at the vertices, with Co atoms at the center of both octahedral and tetrahedral sites. CoS forms an hcp (hexagonal close-packed) structure with CoS_6 octahedra, and Co atoms are positioned at the center of trigonal prisms with sulfur atoms in the CoS_6 octahedra. CoS_6 (octahedra) share corners with the CoS_4 tetrahedra and are isolated from each other, whereas CoS_4 tetrahedra are linked to each other by their edges and corners. When CoS2 is employed as a cathode material for thermal batteries, cobalt disulfide undergoes several phase transformations during the discharge reaction, which are associated with multisteps of voltage plateaus, with each voltage plateau corresponding to the formation of distinct cobalt sulfide compounds. The discharge mechanism is given in eq 4:

$$CoS_2\ (1.6\ V) \rightarrow Co_3S_4 + Li_2S\ (1.4\ V) \rightarrow Co_9S_8 + Li_2S\ (1.2\ V) \rightarrow Co + Li_2S\ (1.1\ V) \quad (4)$$

Table 1 summarizes the list of various TMCs and TMHs employed as cathode materials in thermal batteries. All the phase transformations of chemical reactions have been correlated with the help of a Co−S phase diagram and confirmed with the Payne's powder neutron diffraction pattern.[38] During the CoS_2 cell discharge, the observed electrochemical voltage plateau between 1.8 and 1.6 V corresponds to the phase transformation of CoS_2 to CoS and Li_2S. At 1.6 V, CoS_2 is no longer present in the diffraction pattern; only CoS and Li_2S are observed. The plateau between 1.6 and 1.4 V corresponds to the phase transition of CoS (via CoS_{1-y}) to Co_9S_8. At 1.2 V, the Co_9S_8 phase exists in the diffraction pattern. The final plateau between 1.2 and 1.1 V corresponds to the phase transition of Co_9S_8 to Co. At 1.1 V, only Co exists in the diffraction pattern. The potential below 1.1 V is the cutoff point for practical applications. During discharging, it is found that there is a presence of the hexagonal CoS phase, but there is no evidence for the formation of the Co_3S_4 spinel phase. The sulfur deficiency increases the lattice parameters of the hexagonal CoS crystalline phase. Further discharge leads to the formation of the Co_9S_8 phase with a high sulfur loss, which favors the formation of the Li_2S phase on discharge.[39−41] The newly proposed discharge mechanism is as shown in eqs 5−7:

$$CoS_2 + 2Li \rightarrow CoS + Li_2S \quad (5)$$

$$CoS + 2/9Li \rightarrow 1/9Co_9S_8 + 1/9Li_2S \quad (6)$$

$$1/9Co_9S_8 + 16/9Li \rightarrow Co + 8/9Li_2S \quad (7)$$

The novel CoS_2/CNTs composite and carbon coated CoS_2 material offers a better electronic conductivity and superior pulse discharge over the conventional CoS_2 by preventing the high self-discharge rate and oxidation during air exposure. The CoS_2/CNTs composite developed using a hydrothermal method was found to provide a discharge specific capacity of 215 mA h g^{-1} at a terminating voltage of 1.7 V and exhibited a thermal stability up to 625 °C. After 30 cycles of pulse discharge, 64% of the power was found to be retained at a current density of 500 mA cm^{-2}. During discharge, the carbon

https://doi.org/10.1021/acsomega.3c08809
ACS Omega 2024, 9, 7357−7374

coated CoS_2 cathode revealed superior behavior compared to bare CoS_2 in terms of its discharge capacity and resistance. Bare CoS_2 when exposed to air for a longer period undergoes surface oxidation with moisture absorption, whereas the carbon coated CoS_2 remained unaltered and stable.

Carbon-coated CoS_2, synthesized at 400 °C through pyrolysis using sucrose, outperforms bare CoS_2 due to the prevention of self-discharge reactions by blocking pores of dissoluted anodic Li atom on the CoS_2 cathode material during discharge. It significantly increases the discharge specific capacity to 243 mAh g^{-1} at a current density of 100 mA cm^{-2}, achieving 65% of the theoretical capacity. At 500 mA cm^{-2}, the specific capacity of pristine CoS_2 and carbon-coated CoS_2 is 258 mAh g^{-1} and 283 mAh g^{-1}, respectively. DSC analysis shows that the thermal stability of pristine CoS_2 and CoS_2/C remains unchanged, with an endothermic peak at the same temperature (724 °C). Yu et al. synthesized Fe-doped CoS_2 ($Co_xFe_{1-x}S_2$) materials to enhance the chemical stability of CoS_2 in air exposure. Battery cells with CoS_2 and CoS_2/CNTs at different cutoff voltages exhibited specific capacities. At the highest cutoff voltage of around 1.7 V, the CoS_2 and CoS_2/CNTs battery cell revealed a specific capacity of 200 and 220 mAh g^{-1}, respectively. Moreover, at a low cutoff voltage of 1 V, the CoS_2 and CoS_2/CNTs battery cell revealed a specific capacity of 630 and 668 mAh g^{-1}, respectively.[53,54]

In another approach, nickel sulfides were also employed as cathode materials in thermal battery systems, due to their semiconducting nature and moderate thermal stability (590 °C) existence in various stoichiometric crystalline phases including NiS, NiS_2, Ni_3S_2, Ni_3S_4, Ni_6S_5, Ni_7S_6, and Ni_9S_8. Like other metal sulfides, nickel sulfides face issues such as capacity fading and significant volume expansion during charge/discharge cycles. These shortcomings can lead to cracking, particle pulverization, and loss of contact with current. NiS_2 is considered an attractive cathode material for thermal batteries (theoretical capacity ~870 mAh g^{-1}) due to its inherent thermal and electrochemical performance and cost-effectiveness. A single-phase NiS_2 cathode exhibited a specific capacity of 820 mAh g^{-1}. Nanocrystallization of NiS_2 results in increased density of lattice defects and surface energy, which enhances its electrochemical performance. However, nanocrystallization may slightly reduce the thermal stability of NiS_2.

NiS_2 with a crystallite size of 70 nm exhibited excellent discharge performance at 500 °C, with a specific capacity of 831 mAh g^{-1}, close to its theoretical capacity, at a current density of 0.1 A cm^{-2} and terminate voltage of 0.5 V. Hierarchical carbon modification of NiS_2 increases its thermal decomposition temperature from 400 to 590 °C. The carbon-coated NiS_2 material exhibits improved discharge performance at 500 °C, with a specific capacity of 610 mAh g^{-1}. Multiple shielding effects of carbon modification effectively impede the dissolution and shuttling of sulfide ions, enhance electronic conductivity, and improve thermal stability. The polarization resistance of the carbon-coated NiS_2 cell is approximately 0.27 Ω, which is significantly lower than the 0.54 Ω resistance of the uncoated NiS_2 cell. Thus, nanocrystallization and carbon modification can significantly enhance the performance and thermal stability of NiS_2 as a cathode material in thermal batteries, making it a promising option for practical applications.[55,56]

Due to the superior thermal stability of CoS_2 and NiS_2 relative to FeS_2, and due to the limited formation of sulfur gas during the discharge process, CoS_2 and NiS_2 can be considered as alternate materials for the conventional FeS_2. But their limited availability and high-cost may be considered as impediments in commercializing the CoS_2 thermal battery systems, unless these sulfides are prepared from available secondary sources especially from the spent LIBs.

In another approach, TMHs based cathode materials such as FeF_3, NiF_2, CuF_2, and $NiCl_2$ are employed in thermal batteries. It was found that the pristine FeF_3 provides an initial discharge voltage of 3.20 V and a specific capacity of 82 mAh g^{-1} at a current density of 100 mA cm^{-2} and also is highly thermal stable up to 800 °C, whereas modified FeF_3 with 1 wt % MWCNTs provides an initial discharge voltage of 3.27 V with a specific capacity to 160 mAh g^{-1}.[57]

When $PbCl_2$ was employed as the active cathode material due to its discharge plateau and high utilization rate, it provided a new direction for the development of thermal batteries with chloride-based cathode active material. Moreover, $PbCl_2$ resulted in a discharge specific capacity of 168 mAh g^{-1} at 450 °C and 0.5 C current rate, the voltage plateau reaches 1.8 V, and the active material utilization rate was found to be as high as 87.5% when the cutoff voltage was 0.5 V.[58] Figure 5 displays the requirements essential for high performance cathode materials in thermal batteries.

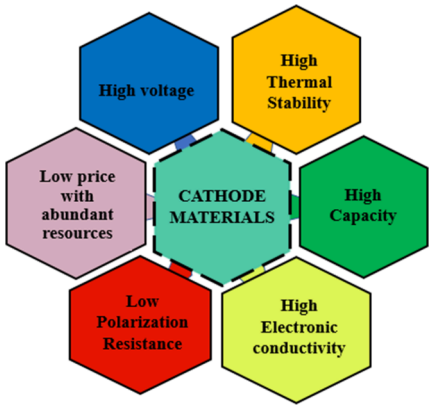

Figure 5. Characteristic properties of cathode materials in thermal batteries.

3. TMCs AND TMHs AS ANODE MATERIALS FOR RECHARGEABLE MONOVALENT METAL-ION BATTERIES

The previous section deliberated the suitability of TMCs as cathode materials in thermal battery systems which operate at temperatures above 500 °C. In this section the utilization of TMCs as anode materials in rechargeable monovalent metal-ion batteries is discussed in detail. Unlike thermal battery systems, where abrupt chemical reactions occur through a reaction of TMCs with Li based alloys, here monovalent metal ion batteries (Li, Na, and K) continuously undergo intercalation and deintercalation within the graphite layers (anode) during electrochemical reactions. Graphite is a suitable anode material for LIBs but is not suitable for the intercalation of larger sodium (Na^+) and potassium (K^+) ions. The larger ionic radii of Na^+ (1.02 Å) and K^+ (1.38 Å) make them less compatible with graphite, which is optimized for lithium (Li^+) ions with a smaller ionic radius (0.76 Å). However, attaining a high energy density of LIBs is still in demand due to the low specific capacity and cyclic stability of

https://doi.org/10.1021/acsomega.3c08809
ACS Omega 2024, 9, 7357−7374

the graphite anode. TMCs are considered as alternative anode materials for LIBs, sodium-ion batteries (SIBs),[59] and potassium-ion batteries (KIBs).[60,61] TMCs are classified as layered metal chalcogenides and nonlayered metal chalcogenides. Layered metal chalcogenides, such as SnS_2, $SnSe_2$, $MoSe_2$, MoS_2, VS_2, and WS_2, are suitable for intercalation-type anode materials and can exhibit excellent lithiation ability and increased specific capacity when compared to graphite. Nonlayered metal chalcogenides, including FeS, FeS_2, $FeSe_2$, CoS_2, $CoSe_2$, NiS_2, Sb_2S_3, and Bi_2S_3, can be used as either a conversion-type anode or cathode materials for these battery systems.[62,63] However, sulfide-based chalcogenides face several challenges during electrochemical reactions, including the shuttle effect (sulfur dissolution), poor electrical conductivity, large volume expansion (the transfer of multiple electrons per metal ion via conversion reaction leads to extended diffusion path length), and sluggish reaction kinetics. During the charge−discharge process in sodium-ion batteries, the formation of sodium suphide (Na_2S) as a reaction intermediate gets solubilized in the electrolyte,[64] leading to material loss.[65−67] To address these issues, various strategies have been attempted, such as wrapping FeS nanoparticles with reduced graphene oxide (rGO) or porous carbon nanosheets, lamination with MnS, and the fabrication of 1D micro-/nanostructured porous FeS/carbon fibers. Other approaches include encapsulating FeS with a 3D carbon nanofiber aerogel and forming yolk−shell FeS_2@C spheres. These nanostructured FeS materials, when combined with a carbon matrix, prevent the shuttle effect, reduce diffusion path lengths, enhance electrical conductivity, increase the interface area between active materials and the electrolyte, and improve reaction kinetics.[68,69]

FeS_2 reaction mechanism are given in eqs 8 and 9:

$$FeS_2 + xe^- + xLi^+ = Li_xFeS_2\ (0 < x < 2;\ 1.5 - 1.7\ V) \quad (8)$$

$$Li_xFeS_2 + (4 - x)Li^+ + (4 - x)e^- = Fe + 2Li_2S\ (\sim 1.5\ V) \quad (9)$$

Micron-sized FeS_2 faces capacity fading issues due to particle pulverization and sulfide exfoliation during charge−discharge cycles. Three different strategies have been employed to mitigate the capacity fading of FeS_2: (1) voltage control: operating the battery in a controlled voltage range (0.5−3 V) to limit the conversion reaction, which can help in maintaining capacity. (2) Use of polyacrylic acid (PAA)-Na binder: replacing traditional binders like PVDF with PAA-Na binder to prevent structural collapse and enhance the stability of FeS_2. (3) Graphene coating: coating FeS_2 with graphene to improve the kinetics of ion intercalation and deintercalation.

Anode materials such as micron-sized FeS_2/carbon nanofiber (m-FeS_2/CNF) and reduced graphene oxide (rGO)-wrapped Fe_3S_4 nanoparticles exhibit high reversible capacity, with 1400 and 950 mAh g^{-1} respectively at a current density of 100 mA g^{-1} over 100 cycles. These materials maintain a capacity of 782 mAh g^{-1} at high current densities (up to 10 A g^{-1}) and are stable up to 800 cycles for LIBs.[70,71]

In the context of sodium ion batteries (SIBs), MoS_2- like layered materials experience sodium ion intercalation during charging (0.4−3 V) and deintercalation during discharging (below 0.4 V)[59]

Na ion intercalation reaction:

$$MoS_2 + e^- + Na^+ = NaMoS_2 \quad (10)$$

Irreversible conversion reaction:

$$NaMoS_2 + xe^- + xNa^+ \rightarrow 2Na_{1+x}MoS_2\ (x \leq 3) \quad (11)$$

$$Na_{1+x}MoS_2 \rightarrow Na_{x-2}MoS_2 + 3e^- + 3Na^+ \quad (12)$$

Reversible conversion reaction:

$$Na_{x-2}MoS_2 + ye^- + yNa^+ = Na_{x+y-2}MoS_2\ (y \leq 3) \quad (13)$$

MoS_2/carbon nanofiber (CNF) anode material exhibited specific capacities of 1220 mAh g^{-1} for LIBs and 450 mAh g^{-1} for SIBs at a current density of 1 A g^{-1} after 1000 cycles. In comparison, bare MoS_2 achieved a specific capacity of 676 mAh g^{-1} for LIBs at the same current density. MoS_2/CNF showed 1.8 times better performance than bare MoS_2 for LIBs. Nanocrystalline $MoSe_2$ displayed a specific capacity of 782 mAh g^{-1} during the initial discharge at a 0.1 C capacity rate for LIBs.[72−74] A uniform coating of SbS_2 (stibnite) on graphene with reduced nanoparticles significantly enhanced the sodium diffusion coefficient and reaction kinetics, and the material exhibited a high capacity of 730 mAh g^{-1} at a current density of 50 mA g^{-1} and retained 95% of its reversible capacity after 50 cycles. These findings highlight the performance of different anode materials in terms of specific capacity, cycling stability, and the impact of various factors such as the addition of carbon nanofibers or graphene coatings. These results suggest that these materials have the potential to improve the efficiency and performance of both LIBs and SIBs.[75]

Cobalt sulfides, a unique class of semiconducting material with various stoichiometric crystalline phases, exhibited specific capacities in the range of 300−800 mAh g^{-1} in LIBs through conversion reactions. However, like iron sulfides, cobalt sulfides also face challenges, including capacity fading, sluggish reaction kinetics, and polysulfide dissolution due to particle pulverization and sulfide disintegration.[76−78] CoS_2 nanospheres have shown a high specific capacity of 800−900 mAh g^{-1} and relatively good cyclic stability, retaining about 75% of their capacity after 500 cycles in LIBs. Co_3S_4 quasi-polyhedron in combination with multiwalled carbon nanotubes (MWCNTs) as nanocomposites have achieved a reversible capacity of 1280 mAh g^{-1} over 50 cycles at 200 mA g^{-1} and 975 mAh g^{-1} over 500 cycles at 2 A g^{-1} in LIBs.[79,80] $Co_{0.85}Se$ microspheres exhibited a specific capacity of 581 mAh g^{-1} during the first cycle but faced capacity retention issues, retaining only 29% of their capacity after 50 cycles in LIBs.[41] CoS_2@Cu_xS nanostructured anode material demonstrated a high specific capacity of 535 mAh g^{-1} at a current density of 0.1 A g^{-1} and 333 mA h g^{-1} at 5 A g^{-1}. It retained 76% of its capacity after 300 cycles in SIBs. Bare CoS_2 exhibited a high specific capacity of 249 mA h g^{-1} at 0.5 A g^{-1} over 1000 cycles in SIBs. These findings illustrate the diverse performance of cobalt sulfides, selenides, and their composites in various battery systems, with some materials exhibiting promising specific capacities and cyclic stability.[81,82]

Nickel sulfides, another class of semiconducting material in various stoichiometric crystalline phases, have also similar challenges such as capacity fading and huge volume expansion issues that attributes to cracking, particle pulverization, and loss of contact with current collectors. Yolk−shell NiS_2 nanoparticles embedded on carbon fibers demonstrated a high specific capacity of 679 mAh g^{-1} at 0.1 C, 245 mAh g^{-1} at

https://doi.org/10.1021/acsomega.3c08809
ACS Omega 2024, 9, 7357−7374

10 C, and excellent cyclic stability of 76% over 5000 cycles for SIBs. $NiS_{1.03}$ hollow spheres and cages achieved a high specific capacity of 127 mAh g^{-1} after 6000 cycles at 8 A g^{-1}. Co/NiSx/C hollow spheres exhibited a high specific capacity of 823 mAh g^{-1} and maintained it over 200 cycles for LIBs. NiSe/C and Ni_3Se_2 nanospheres, used as anode materials for both LIBs and SIBs, displayed a reversible capacity of 400−650 mAh g^{-1} and good cyclic stability of 70%−80% over 100 cycles.[83−85] Copper sulfides are a class of functional semiconductors with various stoichiometric compositions (CuS, $Cu_{1.75}S$, $Cu_{1.8}S$, $Cu_{1.95}S$, Cu_2S, and CuS_2). $Cu_{1.81}S$, as an anode material for SIBs, exhibited a high specific capacity of 331 mAh g^{-1} after 1000 cycles at 3 A g^{-1}.[86−88] $TiSe_2$, used as an anode material, achieved a high specific capacity of 103 mAh g^{-1} at 10 A g^{-1} for SIBs and 75 mAh g^{-1} at a capacity rate of 0.75C for KIBs.[89] VS_2 in the electrolyte of 0.5 M KPF_6 in EC/EDC delivered a high specific capacity of 410 mAh g^{-1} at 0.1 A g^{-1} over 60 cycles and 360 mAh g^{-1} at 0.5 A g^{-1} over 100 cycles for KIBs. V_5S_8/C nanosheets in the electrolyte of 1 M KFSI in EC/PC achieved a high specific capacity of 500 mAh g^{-1} over 100 cycles at 0.05 A g^{-1} and 190 mAh g^{-1} over 1000 cycles at 2 A g^{-1} for KIBs. WS_2/N-doped graphene exhibited a high specific capacity of 900 mA h g^{-1} at 100 mA g^{-1} and maintained 83% of capacity retention for SIBs. WSe_2 achieved a high specific capacity of 498 mA h g^{-1} at 100 mA g^{-1} and maintained 83% of capacity retention for SIBs.[90,91] CuSe nanosheets displayed a high electrochemical reversible capacity of 350 mAh g^{-1} at 0.5 A g^{-1} and retained cycling stability of 92.6% at 2 A g^{-1} for KIBs. MnS on reduced graphene oxide (rGO) sheets revealed high electrochemical performance with specific capacities of 720−847 mAh g^{-1} for both LIBs and SIBs.[92,93]

Sulfides (SnS, Bi_2S_3, and Sb_2S_3) and selenides (SnSe, Bi_2Se_3, and Sb_2Se_3) based chalcogenides are promising anode materials for KIBs. Their electrochemical behavior and reaction mechanisms as anodes can be understood from cyclic voltammetric studies. During a cathodic scan, the following four reduction reactions take place during the initial potassiation process. At a potential of 1.1 V, a secondary electrolyte interface (SEI) layer forms. The potassium conversion reaction takes place at a potential of 1.3 V, resulting in the conversion of $BiSbSe_3$ to $K_3(Bi,Sb)Se_3$ and (Bi,Sb), Another conversion reaction occurs at 0.7 V, leading to the transformation of $K_3(Bi,Sb)Se_3$ to K_2Se and (Bi,Sb). Additionally, alloy formation involving (Bi,Sb) and potassium (K) takes place. In the final stage of reduction, at 0.1 V further alloy formation takes place where K(Bi,Sb) → K_3(Bi,Sb). In the anodic scan, the oxidation peak 0.7 and 1.3 V corresponds to the dealloying reaction where K_3(Bi,Sb) is converted into K(Bi,Sb) and further gets converted to (Bi,Sb), respectively. The oxidation peak at 2.2 V corresponds to the formation of $K_3(Bi,Sb)Se_3$ from the depotassiation of K_2Se and (Bi,Sb).[66]

In another approach, iron trifluoride (FeF_3) is a promising cathode material for both LIBs and NIBs due to its unique electrochemical properties. FeF_3 is known for its high charge transfer capability, making it an excellent candidate for cathodic materials. During the initial stages of intercalation at approximately 3.0 V, FeF_3 undergoes lithiation and forms $LiFeF_3$, providing a specific capacity of 237 mAh g^{-1}. As the electrochemical process continues, FeF_3 can be further lithiated to voltages below 2.0 V. At this stage, $LiFeF_3$ undergoes a conversion reaction, resulting in the decomposition of $LiFeF_3$ into Fe and LiF. This conversion reaction contributes to an extended specific capacity of 475 mAh g^{-1}. The formation of Fe and LiF is characteristic of conversion-type cathode materials, where the material undergoes a significant change in composition during cycling. FeF_3's ecofriendliness and low cost, coupled with its high capacity and stability, make it a promising material for next-generation rechargeable batteries, both in the field of LIBs and SIBs.[59] Its ability to undergo both intercalation and conversion reactions adds to its versatility as a cathode material.[94]

$$FeF_3 + e^- + Li^+ = LiFeF_3 \quad (14)$$

$$LiFeF_3 + 2Li^+ + 2e^- = Fe + 3LiF \quad (15)$$

It was observed that the cosubstitution of Co and O atoms in FeF_3 ($Fe_{0.9}Co_{0.1}OF$) unveiled a high specific capacity of 420 mAh g^{-1} at 70 mA g^{-1} over 330 cycles, or 350 mAh g^{-1} over 1000 cycles at a high rate of 500 mA g^{-1}. Moreover, Co and O substitution in FeF_3, significantly reduced the potential hysteresis to 0.27 V. The performance of $FeF_3{\cdot}0.5H_2O$ and the nanostructured $FeF_3{\cdot}0.5H_2O$-rGO cathode materials displayed a maximum capacity of 135 mAh g^{-1} and 266 mAh g^{-1} respectively, in LIBs. The anhydrate iron fluoride compounds, such as $NaFeF_3$ and FeF_3/C composites, exhibited capacities of 170 and 100 mAh g^{-1}, respectively. The charge transfer resistance of bare $FeF_3{\cdot}0.5H_2O$ is 110 Ω, while the nanostructured $FeF_3{\cdot}0.5H_2O$-rGO is 306 Ω. The $FeF_3{\cdot}3H_2O$/C, $FeF_3{\cdot}0.33H_2O$/C and FeF_3/C nanocomposites were electrochemically tested between the voltage range of 2.0−4.5 V for LIBs. It was found that $FeF_3{\cdot}0.33H_2O$, with an orthorhombic structure with trace amounts of crystal water displayed the best electrochemical performance.[95] $FeF_3{\cdot}0.33H_2O$/C composite delivered an initial discharge capacity of 177 mAh g^{-1} at 0.1 C and 105 mAh g^{-1} at 5 C. After 100 cycles, their capacity retentions remained as high as 83%. Armstrong et al. in their work have enhanced the cathodic efficiency of CoF_2 and FeF_2 nanoparticles in LIBs where CoF_2 revealed a maximum specific capacity of 650 mAh g^{-1} at 1.2 V and FeF_2 revealed a maximum specific capacity of 1100 mAh g^{-1} at 1.0 V. Combining transition metal fluorides with carbon materials, such as C-FeF_2 and C-NiF_2, resulted in different electrochemical performance where C-NiF_2 could exhibit a higher reversible capacity of 350 mAh g^{-1} after 20 cycles compared to C-FeF_2 with a capacity of only 180 mAh g^{-1}. From the cyclic voltammogram readings, it can be understood that NiF_2 nanoparticles revealed a significant reversible peak current density of 0.12 mA g^{-1}, which was not observed in the case of CoF_2 and NH_4MnF_3, which could only provide low current densities (0.08 mA g^{-1} and 0.069 mA g^{-1} respectively). The CNT/CoF_2 multifunctional nanocomposite material provided a specific capacity close to the theoretical value of 500 mAh g^{-1} with a capacity retention of 93% after 200 cycles at 100 mA g^{-1} and maintained nearly 50% even after 10000 cycles at 1000 mA g^{-1}.[96,97]

Although graphite is the commonly employed anode material primarily in the case of LIBs, altogether it can be concluded that TMCs and TMHs can be employed as anode materials for LIBs, SIBs, and KIBs. Unlike the thermal battery systems, here the metal chalcogenides are expected to have superior electronic conductivity, a layered structure (for efficient intercalation and deintercalation of alkali metal ions), and an electrically conducting carbon allotrope coating to prevent any material loss or parasitic reactions for enhanced electrochemical performance. Table 2 summarizes the list of

https://doi.org/10.1021/acsomega.3c08809
ACS Omega 2024, 9, 7357−7374

TMCs and TMHs reported as anode materials for monovalent metal-ion batteries.

Table 2. List of TMCs and TMHs Employed As Anode Materials in Monovalent Metal-Ion Batteries

Sl no:	materials	specific capacity (mAh g^{-1})	current density (A g^{-1})	cycle	reference
1.	SnS_2	767	0.1	50	98
2.	$SnSe_2$	515	0.1	100	99
3.	$MoSe_2$	199	5	10000	100
4.	MoS_2	200	5	10	101
5.	VS_2	350	0.1	500	102
6.	WS_2	215	1	10000	103
7.	FeS_2	609	0.1	100	104
8	$FeSe_2$	222	50	5000	31
9.	CoS_2	112	1	200	105
10.	$CoSe_2$	406	0.1	4500	106
11.	NiS_2	558	1	600	107
12.	Sb_2S_3	652	0.1	60	108
13.	Bi_2S_3	603	0.1 A g^{-1}	100	109
14.	FeF_3	461	0.5	10	110
15.	CoF_2	272	1	1000	111

4. TMCS AND TMHS AS CATHODE MATERIALS FOR RECHARGEABLE MULTIVALENT METAL-ION BATTERIES

The previous sections discussed the TMCs and TMHs as cathode and anode materials for thermal and rechargeable monovalent ion batteries primarily focusing on FeS_2, CoS_2, and NiS_2 based materials. This section will elaborate the utilization of other transition metal chalcogenides such as Ti, V, Sn, Sb and Mo. In multivalent metal ion batteries (like MIBs, AIBs and ZIBs, metal ions like Mg^{2+}, Al^{3+}, and Zn^{2+}) undergo various electrochemical processes, including plating, stripping of the metallic anode, and intercalation/conversion on the cathode. The energy storage mechanism of MIB energy is analogous to the AIBs and ZIBs.[112] Mg^{2+} ions in MIBs have a similar size (0.72 Å), hydrated ionic radii (4.28 Å), and charge density to Li^+ ions used in LIBs. However, not all cathode materials suitable for LIBs work well for MIBs. MIBs are gaining attention due to their high theoretical anodic potential (−2.4 V), cell voltage (3.1 V), specific capacity (2200 mAh g^{-1}), energy density (6.8 kWh kg^{-1}), safety, ecofriendliness, dendrite-free deposition, lightweight properties, and cost-effectiveness and also because of their abundance. A similar intercalation/deintercalation of Mg^{2+} ions takes place within the battery similar to that of LIBs. The primary challenge in MIBs is the sluggish solid-state diffusion kinetics on cathode materials, which leads to a voltage hysteresis loop and incomplete magnesiation. Mg^{2+} ions, with their high charge density, face energy barriers during interfacial charge transfer reactions, resulting in slow diffusion kinetics and ion-ligand pair breakage, which would be as twice as high as monovalent (Li^+, Na^+, and K^+) cations. During, a ion insertion/hopping reaction on the host material, a strong Coulombic interaction generated creates problems to adsorb electrons on the host material. To overcome the cathode material challenges of MIBs, hybrid Mg/Li ion batteries (MLIBs) have emerged as a promising next-generation battery type. MLIBs combine a cathode designed for rapid Li^+ storage, a dendrite-free Mg anode, and a chemically stable Mg^{2+}/Li^+ hybrid electrolyte.[113,114]

A chevral phase Mo_6S_8 was proposed as the first cathode material for MIBs with an organohalo-aluminate based electrolyte. Other cathode materials other than Mo_6S_8 revealed slow kinetics and poor reversibility. When Mg^{2+} ions interact with Mo_6S_8, it forms the $Mg_xMo_3S_4$ phase, and the electrochemical reactions involve charge transfer to the axial surfaces of sulfur material and Mg^{2+} insertion in the inner and outer rings of host Mo_6S_8. Mo_6S_8 also has limitations, including an operating voltage of 1.2 V, specific capacity of 110 mAh g^{-1}, and energy density of 126 Wh kg^{-1}. During the second step of the electrochemical reaction (2nd voltage plateau), reduction of the Mo_6 octahedron takes place with subsequent Mg^{2+} insertion in the outer ring of the host Mo_6S_8. Mai et al. synthesized bimetallic diselenides ($Ni_{0.75}Fe_{0.25}Se_2$) with microflower morphology via a solvothermal method and showed improved electrochemical performance in MIBs.[115] This bimetallic functional behavior promoted fast diffusion kinetics compared with unary $NiSe_2$ and Mo_6S_8 by inducing more redox active sites with an initial discharge capacity of 190 mAh g^{-1} and a 500th cycle's discharge capacity of 150 $mAhg^{-1}$ at a current rate of 20 mAg^{-1}. A TiO_2x nanorod array decorated with polypyrrole encapsulated CoS_2 nanosheets (TiO_2x/CoS_2/PPy) as a cathode for hybrid MLIBs has stable Ti−S bonds on the array of TiO_2x nanorod that can greatly reduce the polysulfide dissolution and prevent the CoS_2 exfoliation, which contributes to the astounding structural and chemical stability, fast charge transfer, and ion insertion/hopping during cycling.[116] Graphene-like G-MoS_2/C sandwich-structured microspheres had a positive effect on promoting ionic conductivity and extending the interlayer distance in G-MoS_2/C. The large interlayer separation improved both charge and ion transfer kinetics in G-MoS_2. As a result, it delivered a magnesium storage capacity of 170 mAh g^{-1} after the 50th cycle, which was 24% lower than its theoretical capacity of 232 mAh g^{-1}.[117,118] In contrast, sandwiched MoS_2/C exhibited a capacity of 119 mAh g^{-1} after 20 cycles. Fast exfoliation of MoS_2 and $MoSe_2$ nanosheets was synthesized via a supercritical fluid (SCF) method. The exfoliated MoS_2 and $MoSe_2$ nanosheets exhibited improved the specific capacity (i.e., 81 mAh g^{-1} during 10th cycle and 55 mAh g^{-1} during fifth cycle at a current density of 20 mA g^{-1}, respectively) compared to pristine MoS_2 and $MoSe_2$. These indicate that exfoliated graphene-like MoS_2 and MoS_2/C cathode materials, as well as MoS_2 and $MoSe_2$ nanosheets, have the potential to enhance the performance of magnesium-ion batteries by improving charge and ion transfer kinetics and achieving higher specific capacities. The WSe_2 cathode in MIBs cell exhibited a maximum reversible capacity of 265 mAh g^{-1} after 100 cycles with an excellent capacity retention of 90% for a current density of 50 mA g^{-1} and 70% for high current density of 500 mA g^{-1}.[119,120] The following Mg^{2+} storage mechanism (eqs 16 and 17) was proposed as follows:

$$(1)\ \text{Cathode: } 6WSe_2 + 4Mg^{2+} + 8e^- \leftrightarrow Mg_4W_6Se_{12} \quad (16)$$

$$(2)\ \text{Anode: } 4Mg \leftrightarrow 4Mg^{2+} + 8e^- \quad (17)$$

A micron sized $TiSe_2$ as a cathode material has a larger interlayer spacing than the size of Mg^{2+} ions, making it favorable for Mg^{2+} ion diffusion. The weak vdW interaction between the basal planes of $TiSe_2$ reduces Coulombic

https://doi.org/10.1021/acsomega.3c08809
ACS Omega 2024, 9, 7357−7374

repulsion among Mg ions, facilitating their diffusion into the interlayers of $TiSe_2$. It exhibits good electronic conductivity, which is essential for efficient charge transfer during the electrochemical reactions. $TiSe_2$ has a small electronegativity when combined with anions, which can be advantageous for the reaction mechanisms in MIBs. It also promotes a fading of electrostatic interactions between Mg^{2+} ions and the host material, allowing for reversible intercalation and deintercalation redox reactions. The development of an MX_2 open-tunnel structure in $TiSe_2$ helps in redistributing the charge and enhancing electronic conductivity. Herein, due to the presence of a large 4p orbital, strong d-p orbital hybridization in $TiSe_2$, resulting from the largely overlapping d and p orbitals, facilitates charge displacement in metal-binding units and supports reversible intercalation/deintercalation redox reactions for Mg^{2+} ions. These insights into $TiSe_2$ as a cathode material may have implications not only for MIBs but also for other multivalent ionic battery systems, such as aluminum-ion batteries (AIBs)[121] and zinc-ion batteries (ZIBs).[122]

Aluminum-ion batteries (AIBs) have been an area of research interest due to their potential for providing a high specific capacity of 2980 mAh g^{-1}, which is attributed to a 3-electron transfer reaction. AIBs offer several advantages, including low cost, high safety, ecofriendliness, nontoxicity, and the potential for high electrochemical energy storage. However, they also face significant challenges, such as low Al^{3+} ionic diffusion, electrode degradation or disintegration, and the formation of a passive oxide layer. One of the key challenges in developing AIBs is finding suitable cathode materials which arise from the characteristics of hydrated Al^{3+} ions, which have a relatively large ionic radius of 4.75 Å compared to other multivalent charge carriers like Zn^{2+}, Mg^{2+}, and Ca^{2+}. As a result, cathode materials need to overcome severe kinetic issues associated with the trivalent Al^{3+} ions and their strong electrostatic interaction with cathode materials. Finding cathode materials that can effectively address these challenges is a critical aspect of advancing AIB technology. Researchers continue to explore various materials and strategies to develop high-performance cathodes for AIBs while mitigating these kinetic issues.[123]

MoS_2 nanosheets on graphene foam as a cathode material for AIBs synthesized via a hydrothermal process extended the interlayer spacing of MoS_2 nanosheets to 1.0 nm, which helped inhibit bulk volume changes of the nanosheets during Al^{3+} ionic interactions. This structural stability increased the number of active sites for Al^{3+} ion storage, reducing diffusion blockades and enhancing Al^{3+} ion retention. The cathode material delivered a specific capacity of 105 mAh g^{-1} after 20 cycles and maintained a capacity of 87 mAh g^{-1} after 120 cycles, even at a high current density of 200 mA g^{-1}. Hydrothermally synthesized MoS_2 microspheres have two distinct active sites (A1 and A2 sites) and were identified for Al^{3+} ions intercalation/deintercalation in the MoS_2 microspheres; i.e., the A1 site corresponds to the S−Mo−S bonding, and the A2 site was associated with a vdW gap. Herein, during the Al^{3+} ion intercalation/deintercalation process, S−Mo−S bonding (A1) sites have a tendency to lose their storage capacity, when they undergo a phase transition, whereas the vdW gap (A2) sites are more stable during (de)intercalation reactions. During the discharge process, Al^{3+} ions initially intercalated at the A1 site and then continued to intercalate at A2 sites. The reverse process of deintercalation from the vdW gap occurred during recharge. A2 sites showed more stable Al^{3+} ion intercalation/deintercalation, resulting in excellent discharge capacity. The AIB exhibited a high Coulombic efficiency and good performance. In S−Mo−S bonding (A1) sites, more electrostatic interaction between S^{2-} anionic and Al^{3+} cationic network attributed to the MoS_2 material's electrochemical polarization and was not found to be favorable for the Al^{3+} reversible intercalation/deintercalation process, which consequently promoted the storage capacity loss and phase transition. Nevertheless, Al^{3+} ions adsorbed at vdW gap (A2) sites (i.e., van der Waals force of attraction with an infinitesimal electrostatic force) contribute to more reversible intercalation/deintercalation.[124] As a result, after 100 cycles, the AIB delivered an excellent discharge capacity of 250 mAh g^{-1} at a current rate of 20 mA g^{-1}, whereas the same AIB delivered a poor discharge capacity of 65 mAh g^{-1} at a current rate of 40 mA g^{-1} after 100 cycles. Al^{3+} ions reaction mechanisms have two vacant sites namely a X-Mo-X (A1) site and vdW site (A2) of MoX_2 (X: S, Se, and Te). $MoSe_2$ exhibited a 95% higher Coulombic efficiency at a current density of 100 mA g^{-1} compared to other MoX_2 materials, indicating its potential as a promising cathode material for AIBs.[125]

Chevral phase Mo_6S_8 particles as cathode materials for AIBs were identified as two distinct Al adsorption sites (AAS) within the chevrel phase Mo_6S_8. These sites differ in size and structural arrangement. AAS-1 consists of eight units of Mo_6S_8 forming a cubic-centered hexahedron, while AAS-2 is smaller and arranged as a face-centered hexahedron. The research revealed that Al^{3+} ions preferentially adsorb to AAS-1 sites due to strong electrostatic interactions between the Al^{3+} ions and AAS-1. As a result, Al^{3+} ions could more readily be stored on AAS-1 sites compared to AAS-2 sites. This preferential adsorption of Al^{3+} ions on the AAS-1 sites had a positive impact on the performance of the AIB. The discharge capacity of Mo_6S_8 promptly stabilized after the first cycle, and the battery maintained a balanced discharge capacity of 70 mAh g^{-1} after 50 cycles. This indicates the stability and reversibility of the Al^{3+} ion intercalation/deintercalation process in the cathode material. The Al^{3+} ions storage mechanism of the chevral phase Mo_6S_8 particles is described in eqs 18 and 19 as follows:

$$\text{(1) Cathode: } 8[Al_2Cl_7]^- + 6e^- + Mo_6S_8 \leftrightarrow Al_2Mo_6S_8 + 14[AlCl_4]^- \quad (18)$$

$$\text{(2) Anode: } Al + 7[AlCl_4]^- \leftrightarrow 4[Al_2Cl_7]^- + 3e^- \quad (19)$$

A composite material consisting of binary metal sulfides (S-NiCo) was produced on reduced graphene oxide (rGO). This composite exhibited a high specific capacity of 248 mAh g^{-1} with nearly 100% Coulombic efficiency at a high current density of 1000 mA g^{-1}. After 100 cycles, it retained a capacity of 83 mAh g^{-1}, indicating good cycling stability.[126] Zhang et al. synthesized a novel cathode material by combining Bi_2S_3 and MoS_2 nanorods through a hydrothermal method for AIBs. This hybrid material exhibited a specific capacity of 133 mA h g^{-1} at a high current density of 1000 mA g^{-1}. The heterojunction between Bi_2S_3 and MoS_2 is believed to enhance structural stability and contribute to the long cyclic life of the AIBs.[125] Wu et al. developed cathode material by coating VS_2 nanosheets with graphene (G-VS_2) for AIBs via a physical deposition route. The modified layered G-VS_2 with an interlayer distance of 5.75 Å demonstrated a specific capacity

https://doi.org/10.1021/acsomega.3c08809
ACS Omega 2024, 9, 7357−7374

of 50 mAh g^{-1} at a current density of 100 mA g^{-1} and maintained 100% Coulombic efficiency after 50 cycles. In comparison, normal VS_2 nanosheets exhibited a lower specific capacity of 22 mAh g^{-1} under the same conditions. This modification improved ion diffusion and promoted electron transport, resulting in better ion diffusion kinetics and reduced polarization resistance. The Al^{3+} ions storage mechanism of G-VS_2 is described in eqs 19 and 20 as follows:

$$(1)\ \text{Cathode: } VS_2 + xAl^{3+} + 3xe^- \leftrightarrow Al_xVS_2 \quad (20)$$

$$(2)\ \text{Anode: } Al + AlCl_4^- \leftrightarrow Al_2Cl_7^- \quad (21)$$

Spinel based cubic $Cu_{0.31}Ti_2S_4$ as a cathode material for AIBs exhibited the performance of Al^{3+} ions intercalation/deintercalation within layered TiS_2, where Al^{3+} ions were predominantly stored in the octahedral sites. An energy barrier was raised during the Al^{3+} insertion and extraction process. This was attributed to the strong Coulombic interaction between the Al^{3+} ions and anionic sulfide sites within the TiS_2 structure. Consequently, AIBs using layered TiS_2 as a cathode material exhibited sluggish diffusion kinetics for the insertion and extraction of Al^{3+} ions. This sluggish diffusion limits the rate at which Al^{3+} ions can move in and out of the cathode material, which, in turn, affects the overall performance of the battery reducing its discharge capacity to 70 mAh g^{-1}.[127]

Zinc-ion batteries have garnered significant attention as energy storage devices due to several favorable characteristics, including their high redox potential (−0.763 V), theoretical volumetric energy density (5855 mAh cm^{-1}), safety, abundance and low cost. Zinc-ion chemistry is suitable for both aqueous and nonaqueous batteries.[128] The ionic conductance of Zn^{2+} in water (1000 mS cm^{-1}) is much greater than organic solvents (1−10 mS cm^{-1}). However, one of the challenges with zinc-ion batteries is the relatively poor diffusion kinetics of Zn^{2+} ions in electrolytes. Zn^{2+} ions tend to coordinate with water molecules in aqueous solutions, leading to reduced mobility.[112,128,129] Liang et al. modified or activated layered MoS_2 by replacing sulfur atoms with oxygen atoms using a hydrothermal method. The introduction of oxygen atoms led to the expansion of the interlayer spacings within the MoS_2 structure, resulting in greater distances between MoS_2 layers (6.2−9.5 Å) subsequently increasing the hydrophilicity and reducing vander wals interaction due to the Mo−O bond formation. Oxygen atoms are smaller than sulfur atoms, and the presence of oxygen significantly improved the diffusion kinetics of Zn^{2+} ions. As a result, of these modifications, the activated MoS_2 material exhibited a higher specific capacity of 232 mAh g^{-1}, representing a 10-fold increase over the unmodified MoS_2.[130] Li et al. developed a novel structure by growing vertically aligned MoS_2 on 3D network of carbon fibers, subsequently expanding the interlayer spacings of MoS_2. This assembled structure provided a larger surface area and improved a better interfacial contact between electrolyte and MoS_2, which expedited the Zn^{2+} diffusion kinetics. The expanded interlayer spacings within the MoS_2 structure helped reduce the energy barrier for Zn^{2+} ion diffusion (zincate formation and the ionic resistance), thereby promoting faster reaction kinetics. As a result, the expanded MoS_2 exhibited a discharge capacity of 200 mAh g^{-1} and impressive capacity retention of 98.6% after 600 cycles demonstrating its suitability for Zinc-ion batteries.[131] The proposed Zn^{2+} storage mechanism is shown in eqs 21 and 22 as follows:

$$(1)\ \text{Cathode: } xZn^{2+} + x2e^- + MoS_2 \leftrightarrow Zn_xMoS_2 \quad (22)$$

$$(2)\ \text{Anode: } xZn + x2e^- \leftrightarrow xZn \quad (23)$$

Xu et al. employed defect engineering techniques to create defect-rich MoS_2 nanosheets through a hydrothermal route with subsequent heat treatment. The introduction of defects, including 100-plane stacking faults and disordered atomic displacement, led to increased surface energy of the MoS_2 nanosheets, making them more favorable for ion adsorption. The defects nucleated new active sites within the material, which could accommodate more ions and improve ion adsorption. Moreover, it could expand the interlayer spacings (6.86 Å) in the MoS_2 structure, facilitating the diffusion of ions within the material. As a result of these defect-induced modifications, the defect-rich MoS_2 nanosheets demonstrated a discharge capacity of 102 mAh g^{-1} after 600 cycles at a high current rate of 500 mA g^{-1}, showcasing improved cycling stability.[132] Yang et al. fabricated novel MoS_2 nanosheets with a porous tubular/layered structure with an interlayer spacings of 6.5 Å, which helped enhance their performance as cathode materials for energy storage. The modified MoS_2 nanosheets demonstrated a specific capacity of 146 mAh g^{-1} and impressive capacity retention of 74% after 800 cycles at a current rate of 200 mA g^{-1}, highlighting their suitability for use as cathode materials in energy storage systems.[133] Table 3 displays the list of various TMCs employed as cathode materials and their electrochemical performance in multivalent metal ion batteries.

Table 3. List of TMCs Employed As Cathode Materials and Their Electrochemical Performance in Multivalent Metal Ion Batteries

s. no.	materials	specific capacity (mAh g^{-1})	current density (A g-1)	cycle	references
1.	MoS_2	119	0.1	50	138
2.	$MoSe_2$	520	2	400	139
3.	WSe_2	265	0.5	100	119
4.	$TiSe_2$	108	5	50	140
5.	VSe_2	240	0.5	40	141
6.	Bi_2S_3	150	0.67	100	109

He et al. prepared VS_2 nanosheets (vanadium-based transition metal dichalcogenides) via a hydrothermal reaction, which are potential candidates for ZIB cathodes. The interlayer spacing of the resulting VS_2 nanosheets was measured to be 5.76 Å, which indicates a reasonably open structure favorable for ion diffusion and intercalation. In ZIB applications, the hydrothermally prepared VS_2 nanosheets exhibited a high specific capacity of 190 mAh g^{-1}, and an impressive 98% capacity retention was observed after 200 charge/discharge cycles at a relatively low current rate of 50 mA g^{-1}. The proposed electrochemical reactions[134] are shown in eqs 23 and 24:

$$(1)\ \text{Cathode: } VS_2 + 0.09Zn^{2+} + 0.18e^- \leftrightarrow Zn_{0.09}VS,Zn_{0.09}VS_2 + 0.14Zn^{2+} + 0.28e^- \leftrightarrow Zn_{0.23}VS_2 \quad (24)$$

$$(2)\ \text{Anode: } Zn^{2+} + 2e^- \leftrightarrow Zn \quad (25)$$

https://doi.org/10.1021/acsomega.3c08809
ACS Omega 2024, 9, 7357−7374

Table 4. Comparison of Various TMCs and TMHs Employed As Cathode and Anode Materials in Thermal, Mono-, and Multivalent Metal Ion Batteries

material	thermal stability (°C)	ohmic resistance (Ω·cm^2)	valency	suitable for thermal (TB)/ secondary battery (SB)	suitable for anode/cathode
FeS_2	550	240	+2	TB, SB	Cathode for TB, Anode for SB
CoS_2	650	50	+2	TB, SB	Cathode
NiS_2	590	4	+2	TB	Cathode
SnS_2	400	300	+4	SB	Anode
TiS_2	400	400	+4	SB	Anode
VS_2	420	6	+5	SB	Anode
WS_2	410	11	+4	SB	Anode
MoS_2	650	25	+4	TB, SB	Cathode
Sb_2S_3	190	30	+3	SB	Anode
Bi_2S_3	685	1800	+3	SB	Anode
$SnSe_2$	680	280	+4	SB	Anode
$MoSe_2$	380	1600	+4	SB	Anode, Cathode
$CoSe_2$	300−550	250	+2	SB	Anode, Cathode
$FeSe_2$	260	40	+2	SB	Anode, Cathode
$NiSe_2$	320	600	+2	SB	Anode
$TiSe_2$	350	290	+4	SB	Cathode
WSe_2	220	900	+4	SB	Cathode
FeF_3	800	40	+3	TB, SB	Cathode for TB, Anode for SB
NiF_2	450	20	+2	TB, SB	Cathode for TB, Anode for SB
CoF_2	500	2	+2	TB, SB	Cathode for TB, Anode for SB

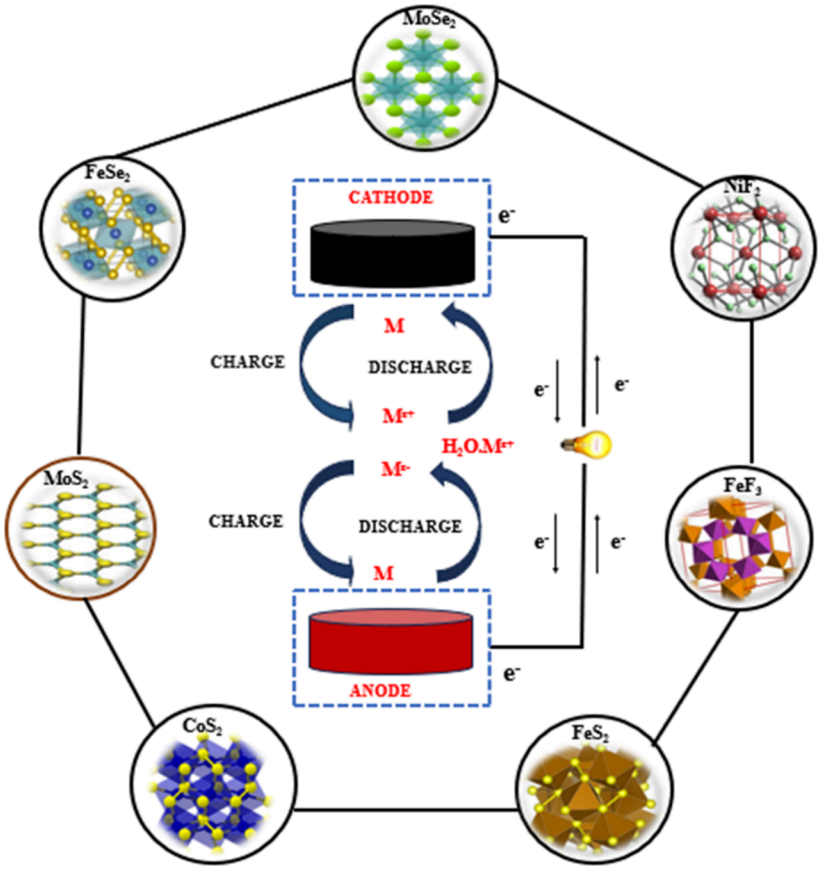

Figure 6. Charge−discharge mechanism in multi- and monovalent metal ion batteries with TMC and TMH based electrode materials.[137]

Jiao et al. developed an open flower structured VS_2 directly on a stainless-steel mesh (VS2@SS) without the need for binder and conductive additives. The free-standing VS_2@SS with interlayer spacings (5.8 Å) promoted the interaction between the electrolyte and active material, which is indicative of a suitable structure for facilitating both ion and charge transfer and shortening the Zn^{2+} diffusion path length. Successively, it is preventing the electrode disintegration by obliging volume expansion. However, the VS_2@SS electrode exhibited a maximum discharge capacity of 198 mAhg^{-1} at 50 mA g^{-1} and outstanding cyclic stability over 2000 cycles at 2000 mA g^{-1}.[135] Wu et al. synthesized ultrathin VSe_2

https://doi.org/10.1021/acsomega.3c08809
ACS Omega 2024, 9, 7357−7374

nanosheets via a wet chemical process. The aqueous ZIB delivered specific capacities of 131, 114, 105, 94, and 79 mAh g^{-1} at various current rates of 100, 200, 500, 1000, and 2000 mA g^{-1}, respectively. When the current density returned to 100 mA g^{-1}, the recovered specific capacity was measured at 118 mAh g^{-1}. Additionally, the VSe_2 nanosheets exhibited a maximum specific capacity of 131 mAh g^{-1} at 100 mA g^{-1} and 80.8% capacity retention after 500 cycles.[135] The possible Zn^{2+} storage mechanisms are shown in eqs 25 and 26 as follows:

$$(1)\ \text{Cathode: } VSe_2 + 0.23Zn^{2+} + 0.46e^- \leftrightarrow Zn_{0.23}VSe_2Zn_{0.23}VSe_2 + 0.17Zn^{2+} + 0.34e^- \leftrightarrow Zn_{0.4}VSe_2 \quad (26)$$

$$(2)\ \text{Anode: } 0.4Zn \leftrightarrow 0.4Zn^{2+} + 0.8e^- \quad (27)$$

Zhu et al. fabricated a crystal chain framework of VS_4 via a hydrothermal method as a cathode material for ZIBs. The VS_4 atomic chain framework is a loosely stacked structure, though the atomic chains are bonded by a weak vdW force and exhibited a capacity of 110 mAh g^{-1} after 500 cycles.[136] The proposed Zn^{2+} reaction mechanisms are shown in eqs 27 and 28:

$$(1)\ \text{Cathode: } VS_4 + 0.49Zn^{2+} + 0.98e^- \leftrightarrow Zn_{0.49}VS_4Zn_{0.49}VS_4 + 0.54Zn^{2+} + 1.08e^- \leftrightarrow Zn_{1.03}VS_4 \quad (28)$$

$$(2)\ \text{Anode: } Zn \leftrightarrow Zn^{2+} + 2e^- \quad (29)$$

Table 4 compares various TMCs and TMHs reported and employed as electrode materials in thermal, mono- and multivalent metal ion batteries. From the table it can be clearly understood that specific physicochemical properties of TMCs and TMHs can be tailored to suit the applications of these materials as either cathodes or anodes in thermal, mono-, and multivalent ion battery systems. Due to the fascinating physicochemical properties leading to attractive electrochemical properties, the structural properties of the transition metal chalcogenides and fluorides can be tailor made to suit and further enhance the voltage stability and specific energy of the primary and secondary batteries. Since the availability of the raw materials is a concern for making transition metal chalcogenides and fluorides involving metals such as Ni, Co, Mo, and W, exploration of extracting these metal values from secondary sources will play a crucial role in sustainable development of next generation batteries.

5. SUMMARY AND OUTLOOK

To be noted, in thermal batteries since conversion reactions at higher temperatures play a crucial role in defining the performance of the system, the material is expected to have high thermal stability, low dissolution in the molten electrolyte accompanied by multiphases during the discharge reaction at higher temperatures, and hence TMCs and TMHs have either a layered or nonlayered structure. On the other hand, since the monovalent energy storage systems involve an intercalation and deintercalation mechanism, for a material to be ideally suited as electrode material, it is expected to possess a layered structure to facilitate inward and outward diffusion of the monovalent ions with higher electrical conductivity; hence,

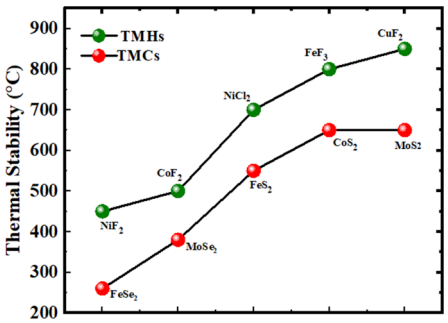

Figure 7. Thermal stability plot of different TMC and TMH electrode materials for mono-/multivalent metal ion batteries. The data from the plot were been taken from Yoon et al. (2019).[142]

TMCs and TMHs are employed as anode materials with a carbon allotrope coating, whereas the multivalent energy storage systems employ TMCs and TMHs with higher valence and multivalent oxidation states, which is expected to resist the stronger field produced during the interaction of di- and trivalent ions with the cathode material facilitating higher energy density with minimal structural and volume changes at a high rate of discharge.

AUTHOR INFORMATION

Corresponding Authors

Premnath Muthu − *Electroplating Metal Finishing Division, CSIR-Central Electrochemical Research Institute, Karaikudi 630003 Tamil Nadu, India*; Email: prem412115005@gmail.com

Loganathan Sadhasivam − *Defence Research and Development Organisation-RCI, Hyderabad 500069 Telangana, India*; Email: loganathans@rcilab.in

Naveen Chandrasekaran − *Electroplating Metal Finishing Division, CSIR-Central Electrochemical Research Institute, Karaikudi 630003 Tamil Nadu, India*; orcid.org/0000-0002-7565-1065; Email: naveen@cecri.res.in, naveenumr@gmail.com

Authors

Sudha Rajagopal − *Electroplating Metal Finishing Division, CSIR-Central Electrochemical Research Institute, Karaikudi 630003 Tamil Nadu, India*

Devishree Saju − *Electroplating Metal Finishing Division, CSIR-Central Electrochemical Research Institute, Karaikudi 630003 Tamil Nadu, India*

Vidyashri Kesavan − *Electroplating Metal Finishing Division, CSIR-Central Electrochemical Research Institute, Karaikudi 630003 Tamil Nadu, India*

Arun Dellus − *Electroplating Metal Finishing Division, CSIR-Central Electrochemical Research Institute, Karaikudi 630003 Tamil Nadu, India*

Complete contact information is available at: https://pubs.acs.org/10.1021/acsomega.3c08809

Notes

The authors declare no competing financial interest.

ACKNOWLEDGMENTS

The authors thank Director-CSIR-CECRI and Er. Loganathan, Scientist-F, DRDO-RCI for their continuous support. Manu-

https://doi.org/10.1021/acsomega.3c08809
ACS Omega 2024, 9, 7357−7374

script Communication Number : CECRI/PESVC/Pubs/2024-005

REFERENCES

(1) Chen, B.; Chao, D.; Liu, E.; Jaroniec, M.; Zhao, N.; Qiao, S. Z. Transition Metal Dichalcogenides for Alkali Metal Ion Batteries: Engineering Strategies at the Atomic Level. *Energy and Environmental Science* **2020**, *13*, 1096−1131.

(2) Yuan, H.; Kong, L.; Li, T.; Zhang, Q. A Review of Transition Metal Chalcogenide/Graphene Nanocomposites for Energy Storage and Conversion. *Chin. Chem. Lett.* **2017**, *28* (12), 2180−2194.

(3) Choi, W.; Choudhary, N.; Han, G. H.; Park, J.; Akinwande, D.; Lee, Y. H. Recent Development of Two-Dimensional Transition Metal Dichalcogenides and Their Applications. *Materials Today* **2017**, *20*, 116−130, DOI: 10.1016/j.mattod.2016.10.002.

(4) Wu, W.; Wang, L.; Li, Y.; Zhang, F.; Lin, L.; Niu, S.; Chenet, D.; Zhang, X.; Hao, Y.; Heinz, T. F.; Hone, J.; Wang, Z. L. Piezoelectricity of Single-Atomic-Layer MoS2 for Energy Conversion and Piezotronics. *Nature* **2014**, *514* (7253), 470−474.

(5) Chhowalla, M.; Shin, H. S.; Eda, G.; Li, L. J.; Loh, K. P.; Zhang, H. The Chemistry of Two-Dimensional Layered Transition Metal Dichalcogenide Nanosheets. *Nat. Chem.* **2013**, *5*, 263−275.

(6) Xu, J.; Zhang, J.; Zhang, W.; Lee, C. S. Interlayer Nanoarchitectonics of Two-Dimensional Transition-Metal Dichalcogenides Nanosheets for Energy Storage and Conversion Applications. *Advanced Energy Materials* **2017**, *7*, No. 1700571, DOI: 10.1002/aenm.201700571.

(7) Huang, X.; Zeng, Z.; Zhang, H. Metal Dichalcogenide Nanosheets: Preparation, Properties and Applications. *Chem. Soc. Rev.* **2013**, *42* (5), 1934−1946.

(8) Li, Y.; Wu, F.; Qian, J.; Zhang, M.; Yuan, Y.; Bai, Y.; Wu, C. Metal Chalcogenides with Heterostructures for High-Performance Rechargeable Batteries. *Small Science* **2021**, *1*, No. 2100012, DOI: 10.1002/smsc.202100012.

(9) Lee, A.; Vörös, M.; Dose, W. M.; Niklas, J.; Poluektov, O.; Schaller, R. D.; Iddir, H.; Maroni, V. A.; Lee, E.; Ingram, B.; Curtiss, L. A.; Johnson, C. S. Photo-Accelerated Fast Charging of Lithium-Ion Batteries. *Nat. Commun.* **2019**, *10* (1), 4946 DOI: 10.1038/s41467-019-12863-6.

(10) Zhou, J.; Qin, J.; Guo, L.; Zhao, N.; Shi, C.; Liu, E. Z.; He, F.; Ma, L.; Li, J.; He, C. Scalable Synthesis of High-Quality Transition Metal Dichalcogenide Nanosheets and Their Application as Sodium-Ion Battery Anodes. *J. Mater. Chem. A Mater.* **2016**, *4* (44), 17370−17380.

(11) Truong, Q. D.; Kempaiah Devaraju, M.; Tran, P. D.; Gambe, Y.; Nayuki, K.; Sasaki, Y.; Honma, I. Unravelling the Surface Structure of MgMn2O4 Cathode Materials for Rechargeable Magnesium-Ion Battery. *Chem. Mater.* **2017**, *29* (15), 6245−6251.

(12) Zhang, W.; Liu, Y.; Guo, Z. Approaching High-Performance Potassium-Ion Batteries via Advanced Design Strategies and Engineering. *Sci. Adv.* **2019**, *5*, DOI: 10.1126/sciadv.aav7412.

(13) Guidotti, R. A.; Masset, P. J. Thermally Activated ("thermal") Battery Technology. Part IV. Anode Materials. *J. Power Sources* **2008**, *183* (1), 388−398.

(14) Guidotti, R. A.; Masset, P. Thermally Activated ("thermal") Battery Technology. Part I: An Overview. *J. Power Sources* **2006**, *161* (2), 1443−1449.

(15) Guidotti, R. A.; Reinhardt, F. W.; Dai, J.; Reisner, D. E. Performance of Thermal Cells and Batteries Made with Plasma-Sprayed Cathodes and Anodes. *J. Power Sources* **2006**, *160* (2 SPEC. ISS.), 1456−1464.

(16) Cho, J. H.; Im, C. N.; Choi, C. H.; Ha, S. H.; Yoon, H. K.; Choi, Y.; Bae, J. Thermal Stability Characteristics of High-Power, Large-Capacity, Reserve Thermal Batteries with Pure Li and Li(Si) Anodes. *Electrochim. Acta* **2020**, *353*, No. 136612, DOI: 10.1016/j.electacta.2020.136612.

(17) Choi, Y. S.; Yu, H. R.; Cheong, H. W. Electrochemical Properties of a Lithium-Impregnated Metal Foam Anode for Thermal Batteries. *J. Power Sources* **2015**, *276*, 102−104.

(18) Li, R.; Guo, W.; Qian, Y. Recent Developments of Cathode Materials for Thermal Batteries. *Frontiers in Chemistry* **2022**, *10*, No. 2022.832972, DOI: 10.3389/fchem.2022.832972.

(19) Ko, J.; Kang, S. H.; Cheong, H. W.; Yoon, Y. S. Recent Progress in Cathode Materials for Thermal Batteries. *Journal of the Korean Ceramic Society* **2019**, *56* (3), 233−255.

(20) Tian, Q.; Wang, J.; Xiang, W.; Zhao, J.; Guo, H.; Hu, J.; Han, X.; Hu, W. Fabrication of the Ni-$NiCl_2$ Composite Cathode Material for Fast-Response Thermal Batteries*Front Chem.* **2021**, *9*, DOI: 10.3389/fchem.2021.679231.

(21) Tian, Q.; Hu, J.; Tang, L.; Guo, H.; Dong, Q.; Wang, J.; Han, X.; Hu, W. A Novel $NiCl_2$-Based Cathode Material for High-Voltage Thermal Battery. *Mater. Lett.* **2021**, *301*, DOI: 10.1016/j.matlet.2021.130272.

(22) Masset, P. J.; Guidotti, R. A. Thermal Activated ("thermal") Battery Technology. Part IIIb. Sulfur and Oxide-Based Cathode Materials. *J. Power Sources* **2008**, *178*, 456−466.

(23) Chang, K.; Chen, W.; Ma, L.; Li, H.; Li, H.; Huang, F.; Xu, Z.; Zhang, Q.; Lee, J. Y. Graphene-like MoS2/Amorphous Carbon Composites with High Capacity and Excellent Stability as Anode Materials for Lithium Ion Batteries. *J. Mater. Chem.* **2011**, *21* (17), 6251−6257.

(24) Wang, P. P.; Sun, H.; Ji, Y.; Li, W.; Wang, X. Three-Dimensional Assembly of Single-Layered Mos2. *Adv. Mater.* **2014**, *26* (6), 964−969.

(25) Ren, W.; Zhang, H.; Guan, C.; Cheng, C. Ultrathin MoS_2 Nanosheets@Metal Organic Framework-Derived N-Doped Carbon Nanowall Arrays as Sodium Ion Battery Anode with Superior Cycling Life and Rate Capability. *Adv. Funct Mater.* **2017**, *27* (32), 1702116 DOI: 10.1002/adfm.201702116.

(26) Ge, Y. X.; Luo, C. X.; Zheng, X.; Liu, J. K. CoxNi1-XCl_2 Allomeric Nanosheets with High Specific Surface Area and Excellent Energy Storage Performance for Cathode Materials of Thermal Batteries. *J. Power Sources* **2023**, *584*, 233598 DOI: 10.1016/j.jpowsour.2023.233598.

(27) Ennaoui, A.; Fiechter, S.; Pettenkofer, C.; Alonso-Vante, N.; Bilker, K.; Bronold, M.; Tributsch, H. Iron Disulfide for Solar Energy Conversion. *Solar Energy Materials and Solar Cells* **1993**, *29*, 289 DOI: 10.1016/0927-0248(93)90095-K.

(28) Masset, P. J.; Guidotti, R. A. Thermal Activated ("thermal") Battery Technology. Part IIIa: FeS2 Cathode Material. *J. Power Sources* **2008**, *177*, 595−609.

(29) Masset, P. J. Thermal Stability of FeS_2 Cathode Material in "Thermal" Batteries: Effect of Dissolved Oxides in Molten Salt Electrolytes. *Z. Naturforschung A* **2008**, *63*, 596 DOI: 10.1313/zna-2008-0911.

(30) Ko, J.; Kim, I. Y.; Jung, H. M.; Cheong, H.; Yoon, Y. S. Thin Cathode for Thermal Batteries Using a Tape-Casting Process. *Ceram. Int.* **2017**, *43* (7), 5789−5793.

(31) Zou, J.; Zhao, J.; Wang, B.; Chen, S.; Chen, P.; Ran, Q.; Li, L.; Wang, X.; Yao, J.; Li, H.; Huang, J.; Niu, X.; Wang, L. Unraveling the Reaction Mechanism of FeS2as a Li-Ion Battery Cathode. *ACS Appl. Mater. Interfaces* **2020**, *12* (40), 44850−44857.

(32) Park, J. S.; Lee, S. M.; Han, Y. S.; Hwang, H. J.; Ryu, S. S. Effects of Debinding Atmosphere on Properties of Sintered Reaction-Bonded Si3N4 Prepared by Tape Casting Method. *Journal of the Korean Ceramic Society* **2016**, *53* (6), 622−627.

(33) Thu, T. L. T.; Thu, T. L. T.; Manh, T. D.; Tan, T. T.; Chang, J. K. An Assessment of Pyrite Thin-Film Cathode Characteristics for Thermal Batteries by the Doctor Blade Coating Method. *Journal of Materials Research and Technology* **2021**, *13*, 1139−1149.

(34) Akbulut, H.; Nalci, D.; Guler, A.; Duman, S.; Guler, M. O. Carbon-Silicon Composite Anode Electrodes Modified with MWCNT for High Energy Battery Applications. *Appl. Surf. Sci.* **2018**, *446*, 222−229.

(35) Lee, Y. N.; Woo, S. P.; Yoon, Y. S.; Kim, S. H. Significant Improvement in Reversibility of MWCNT-Sn Compound Composite Electrode: Nanostructure Effect of MWCNT-Sn Compound

https://doi.org/10.1021/acsomega.3c08809
ACS Omega 2024, 9, 7357−7374

Composite on High Initial Reversible Capacity. *J. Alloys Compd.* **2019**, *777*, 1098−1107.
(36) Rasiyah, P.; Tseung, A. C. C. Reactions of FeS_2, CoS_2, and NiS_2 Electrodes in Molten LiCl-KCl Electrolytes You May Also like A Mechanistic Study of Oxygen Evolution on LiDoped Co. *J. Electrocehm. Soc.* **1983**, *130*, 264.
(37) Yu, X. Y.; Yu, L.; Lou, X. W. Metal Sulfide Hollow Nanostructures for Electrochemical Energy Storage. *Adv. Energy Mater.* **2016**, *6* (3), 1501333 DOI: 10.1002/aenm.201501333.
(38) Payne, J. L.; Percival, J. D.; Giagloglou, K.; Crouch, C. J.; Carins, G. M.; Smith, R. I.; Gover, R. K. B.; Irvine, J. T. S. In Situ Thermal Battery Discharge Using CoS 2 as a Cathode Material. *J. Electrochem. Soc.* **2019**, *166* (12), A2660−A2664.
(39) Wang, Y.; Wu, J.; Tang, Y.; Lü, X.; Yang, C.; Qin, M.; Huang, F.; Li, X.; Zhang, X. Phase-Controlled Synthesis of Cobalt Sulfides for Lithium Ion Batteries. *ACS Appl. Mater. Interfaces* **2012**, *4* (8), 4246−4250.
(40) Jin, R.; Zhou, J.; Guan, Y.; Liu, H.; Chen, G. Mesocrystal Co9S8 Hollow Sphere Anodes for High Performance Lithium Ion Batteries. *J. Mater. Chem. A Mater.* **2014**, *2* (33), 13241−13244.
(41) Wang, Q.; Jiao, L.; Han, Y.; Du, H.; Peng, W.; Huan, Q.; Song, D.; Si, Y.; Wang, Y.; Yuan, H. CoS2 Hollow Spheres: Fabrication and Their Application in Lithium-Ion Batteries. *J. Phys. Chem. C* **2011**, *115* (16), 8300−8304.
(42) Choi, Y.; Cho, S.; Lee, Y. S. Effect of the Addition of Carbon Black and Carbon Nanotube to FeS2 Cathode on the Electrochemical Performance of Thermal Battery. *Journal of Industrial and Engineering Chemistry* **2014**, *20* (5), 3584−3589.
(43) Oh, I.; Cho, J.; Kim, K.; Ko, J.; Cheong, H.; Yoon, Y. S.; Jung, H. M. Poly(Imide-Co-Siloxane) as a Thermo-Stable Binder for a Thin Layer Cathode of Thermal Batteries. *Energies (Basel)* **2018**, *11* (11). DOI: 10.3390/en11113154.
(44) Xie, S.; Deng, Y.; Mei, J.; Yang, Z.; Lau, W. M.; Liu, H. Facile Synthesis of CoS2/CNTs Composite and Its Exploitation in Thermal Battery Fabrication. *Compos B Eng.* **2016**, *93*, 203−209.
(45) Hu, J.; Chu, Y.; Tian, Q.; Wang, J.; Li, Y.; Wu, Q.; Zhao, L.; Zhu, Y. Film Cathode for Thermal Batteries Using a Screen-Printing Process. *Mater. Lett.* **2018**, *215*, 296−299.
(46) Jin, C.; Zhou, L.; Fu, L.; Zhu, J.; Li, D.; Yang, W. The Acceleration Intermediate Phase (NiS and Ni3S2) Evolution by Nanocrystallization in Li/NiS2 Thermal Batteries with High Specific Capacity. *J. Power Sources* **2017**, *352*, 83−89.
(47) Zheng, X.; Zhu, Y.; Sun, Y.; Jiao, Q. Hydrothermal Synthesis of MoS2 with Different Morphology and Its Performance in Thermal Battery. *J. Power Sources* **2018**, *395*, 318−327.
(48) Guo, S.; Guo, H.; Wang, X.; Zhu, Y.; Yang, M.; Zhang, Q.; Chu, Y.; Wang, J. Synthesis and Electrochemical Performance of WS2 Nanosheet for Thermal Batteries. *Mater. Lett.* **2019**, *249*, 81−83.
(49) Guo, S. N.; Guo, H.; Wang, X.; Zhu, Y.; Hu, J.; Yang, M.; Zhao, L.; Wang, J. Iron Trifluoride as a High Voltage Cathode Material for Thermal Batteries. *J. Electrochem. Soc.* **2019**, *166* (15), A3599−A3605.
(50) Chang, Q.; Luo, Z.; Fu, L.; Zhu, J.; Yang, W.; Li, D.; Zhou, L. A New Cathode Material of NiF_2 for Thermal Batteries with High Specific Power. *Electrochim. Acta* **2020**, *361*, 137051 DOI: 10.1016/j.electacta.2020.137051.
(51) Wang, L.; Wu, Z.; Zou, J.; Gao, P.; Niu, X.; Li, H.; Chen, L. Li-Free Cathode Materials for High Energy Density Lithium Batteries. *Joule* **2019**, *3*, 2086−2102, DOI: 10.1016/j.joule.2019.07.011.
(52) Hu, J.; Chu, Y.; Tian, Q.; Guo, S.; Yang, M.; Wang, X.; Zhao, L.; Zhu, Y. Electrochemical Properties of the $NiCl_2$ Cathode with Nickel Foam Substrate for Thermal Batteries. *Mater. Lett.* **2017**, *207*, 198−201.
(53) Xie, S.; Deng, Y.; Mei, J.; Yang, Z.; Lau, W. M.; Liu, H. Carbon Coated CoS2 Thermal Battery Electrode Material with Enhanced Discharge Performances and Air Stability. *Electrochim. Acta* **2017**, *231*, 287−293.
(54) Xie, S.; Deng, Y.; Mei, J.; Yang, Z.; Lau, W. M.; Liu, H. Facile Synthesis of CoS2/CNTs Composite and Its Exploitation in Thermal Battery Fabrication. *Compos B Eng.* **2016**, *93*, 203−209.
(55) Jin, C.; Zhou, L.; Fu, L.; Zhu, J.; Li, D.; Yang, W. The Acceleration Intermediate Phase (NiS and Ni3S2) Evolution by Nanocrystallization in Li/NiS2 Thermal Batteries with High Specific Capacity. *J. Power Sources* **2017**, *352*, 83−89.
(56) Jin, C.; Fu, L.; Zhu, J.; Yang, W.; Li, D.; Zhou, L. A Hierarchical Carbon Modified Nano-NiS2 Cathode with High Thermal Stability for a High Energy Thermal Battery. *J. Mater. Chem. A Mater.* **2018**, *6* (16), 7123−7132.
(57) Guo, S. N.; Guo, H.; Wang, X.; Zhu, Y.; Hu, J.; Yang, M.; Zhao, L.; Wang, J. Iron Trifluoride as a High Voltage Cathode Material for Thermal Batteries. *J. Electrochem. Soc.* **2019**, *166* (15), A3599−A3605.
(58) Chen, F.; Jiang, C.; Xu, L.; Li, X.; Shen, Q. High Utilization Rate Thermal Batteries Using $PbCl_2$ as a Cathode Material. *Mater. Lett.* **2021**, *299*, 130018 DOI: 10.1016/j.matlet.2021.130018.
(59) Wang, M.; Wang, Q.; Ding, X.; Wang, Y.; Xin, Y.; Singh, P.; Wu, F.; Gao, H. The Prospect and Challenges of Sodium-ion Batteries for Low-temperature Conditions. *Interdisciplinary Materials* **2022**, *1* (3), 373−395.
(60) Bonaccorso, F.; Colombo, L.; Yu, G.; Stoller, M.; Tozzini, V.; Ferrari, A. C.; Ruoff, R. S.; Pellegrini, V. Graphene, Related Two-Dimensional Crystals, and Hybrid Systems for Energy Conversion and Storage. *Science* **2015**, *347*, DOI: 10.1126/science.1246501.
(61) He, G.; Kan, W. H.; Manthiram, A. A 3.4 v Layered VOPO4 Cathode for Na-Ion Batteries. *Chem. Mater.* **2016**, *28* (2), 682−688.
(62) Chang, K.; Chen, W. L -Cysteine-Assisted Synthesis of Layered MoS2/Graphene Composites with Excellent Electrochemical Performances for Lithium Ion Batteries. *ACS Nano* **2011**, *5* (6), 4720−4728.
(63) Chang, K.; Chen, W. In Situ Synthesis of MoS2/Graphene Nanosheet Composites with Extraordinarily High Electrochemical Performance for Lithium Ion Batteries. *Chem. Commun.* **2011**, *47* (14), 4252−4254.
(64) Li, C.; Li, R.; Liu, K.; Si, R.; Zhang, Z.; Hu, Y. NaSICON: A Promising Solid Electrolyte for Solid-state Sodium Batteries. *Interdisciplinary Materials* **2022**, *1* (3), 396−416.
(65) Hwang, H.; Kim, H.; Cho, J. MoS2 Nanoplates Consisting of Disordered Graphene-like Layers for High Rate Lithium Battery Anode Materials. *Nano Lett.* **2011**, *11* (11), 4826−4830.
(66) Zhou, P.; Collins, G.; Hens, Z.; Ryan, K. M.; Geaney, H.; Singh, S. Colloidal WSe2nanocrystals as Anodes for Lithium-Ion Batteries. *Nanoscale* **2020**, *12* (43), 22307−22316.
(67) Lian, R.; Wang, D.; Ming, X.; Zhang, R.; Wei, Y.; Feng, J.; Meng, X.; Chen, G. Phase Transformation, Ionic Diffusion, and Charge Transfer Mechanisms of $KVOPO_4$ in Potassium Ion Batteries: First-Principles Calculations. *J. Mater. Chem. A Mater.* **2018**, *6* (33), 16228−16234.
(68) Palchoudhury, S.; Ramasamy, K.; Han, J.; Chen, P.; Gupta, A. Transition Metal Chalcogenides for Next-Generation Energy Storage. *Nanoscale Advances* **2023**, *5*, 2724−2742, DOI: 10.1039/d2na00944g.
(69) Wu, C.; Maier, J.; Yu, Y. Generalizable Synthesis of Metal-Sulfides/Carbon Hybrids with Multiscale, Hierarchically Ordered Structures as Advanced Electrodes for Lithium Storage. *Adv. Mater.* **2016**, *28* (1), 174−180.
(70) Sun, D.; Wang, L.; Li, Y.; Yang, Y.; Zhou, X.; Ma, G.; Lei, Z. Confined Metal Sulfides Nanoparticles into Porous Carbon Nanosheets with Surface-Controlled Reactions for Fast and Stable Lithium-Ion Batteries. *ChemElectroChem.* **2019**, *6* (17), 4464−4470.
(71) Fan, H. H.; Li, H. H.; Huang, K. C.; Fan, C. Y.; Zhang, X. Y.; Wu, X. L.; Zhang, J. P. Metastable Marcasite-FeS2 as a New Anode Material for Lithium Ion Batteries: CNFs-Improved Lithiation/Delithiation Reversibility and Li-Storage Properties. *ACS Appl. Mater. Interfaces* **2017**, *9* (12), 10708−10716.
(72) Wu, X.; Zhao, H.; Xu, J.; Wang, Y.; Dai, S.; Xu, T.; Liu, S.; Zhang, S.; Wang, X.; Li, X. Rational Synthesis of Marcacite FeS2 Hollow Microspheres for High-Rate and Long-Life Sodium Ion Battery Anode. *J. Alloys Compd.* **2020**, *825*, No. 154173, DOI: 10.1016/j.jallcom.2020.154173.
(73) Dai, S.; Wang, L.; Cao, M.; Zhong, Z.; Shen, Y.; Wang, M. Design Strategies in Metal Chalcogenides Anode Materials for High-

https://doi.org/10.1021/acsomega.3c08809
ACS Omega 2024, 9, 7357−7374

Performance Sodium-Ion Battery. *Materials Today Energy* **2019**, *12*, 114−128, DOI: 10.1016/j.mtener.2018.12.011.
(74) Jung, J. W.; Ryu, W. H.; Yu, S.; Kim, C.; Cho, S. H.; Kim, I. D. Dimensional Effects of MoS2 Nanoplates Embedded in Carbon Nanofibers for Bifunctional Li and Na Insertion and Conversion Reactions. *ACS Appl. Mater. Interfaces* **2016**, *8* (40), 26758−26768.
(75) Wang, H.; Wang, X.; Wang, L.; Wang, J.; Jiang, D.; Li, G.; Zhang, Y.; Zhong, H.; Jiang, Y. Phase Transition Mechanism and Electrochemical Properties of Nanocrystalline MoSe2 as Anode Materials for the High Performance Lithium-Ion Battery. *J. Phys. Chem. C* **2015**, *119* (19), 10197−10205.
(76) Yu, D. Y. W.; Prikhodchenko, P. V.; Mason, C. W.; Batabyal, S. K.; Gun, J.; Sladkevich, S.; Medvedev, A. G.; Lev, O. High-Capacity Antimony Sulphide Nanoparticle-Decorated Graphene Composite as Anode for Sodium-Ion Batteries. *Nat. Commun.* **2013**, *4*, 2922 DOI: 10.1038/ncomms3922.
(77) Gu, Y.; Xu, Y.; Wang, Y. Graphene-Wrapped CoS Nanoparticles for High-Capacity Lithium-Ion Storage. *ACS Appl. Mater. Interfaces* **2013**, *5* (3), 801−806.
(78) Kong, S.; Jin, Z.; Liu, H.; Wang, Y. Morphological Effect of Graphene Nanosheets on Ultrathin CoS Nanosheets and Their Applications for High-Performance Li-Ion Batteries and Photocatalysis. *J. Phys. Chem. C* **2014**, *118* (44), 25355−25364.
(79) Yu, J.; Li, X.; Sun, Y.; Liu, X. CoS@sulfur Doped Onion-like Carbon Nanocapsules with Excellent Cycling Stability and Rate Capability for Sodium-Ion Batteries. *Ceram. Int.* **2018**, *44* (14), 17113−17117.
(80) Dong, C.; Guo, L.; He, Y.; Shang, L.; Qian, Y.; Xu, L. Ultrafine Co1-: XS Nanoparticles Embedded in a Nitrogen-Doped Porous Carbon Hollow Nanosphere Composite as an Anode for Superb Sodium-Ion Batteries and Lithium-Ion Batteries. *Nanoscale* **2018**, *10* (6), 2804−2811.
(81) Tian, R.; Zhou, Y.; Duan, H.; Guo, Y.; Li, H.; Chen, K.; Xue, D.; Liu, H. MOF-Derived Hollow Co3S4 Quasi-Polyhedron/MWCNT Nanocomposites as Electrodes for Advanced Lithium Ion Batteries and Supercapacitors. *ACS Appl. Energy Mater.* **2018**, *1* (2), 402−410.
(82) Zhou, J.; Wang, Y.; Zhang, J.; Chen, T.; Song, H.; Yang, H. Y. Two Dimensional Layered Co0.85Se Nanosheets as a High-Capacity Anode for Lithium-Ion Batteries. *Nanoscale* **2016**, *8* (32), 14992−15000.
(83) Fang, Y.; Luan, D.; Chen, Y.; Gao, S.; Lou, X. W. David Synthesis of Copper-Substituted CoS 2 @Cu x S Double-Shelled Nanoboxes by Sequential Ion Exchange for Efficient Sodium Storage. *Angew. Chem.* **2020**, *132* (7), 2666−2670.
(84) Li, Z.; Feng, W.; Lin, Y.; Liu, X.; Fei, H. Flaky CoS2 and Graphene Nanocomposite Anode Materials for Sodium-Ion Batteries with Improved Performance. *RSC Adv.* **2016**, *6* (74), 70632−70637.
(85) Zhang, Y.; Zhou, Q.; Zhu, J.; Yan, Q.; Dou, S. X.; Sun, W. Nanostructured Metal Chalcogenides for Energy Storage and Electrocatalysis. *Advanced Functional Materials* **2017**, *27*, No. 1702317, DOI: 10.1002/adfm.201702317.
(86) Li, T.; Li, H.; Qin, A.; Wu, H.; Zhang, D.; Xu, F. Assembled NiS Nanoneedles Anode for Na-Ion Batteries: Enhanced the Performance by Organic Hyperbranched Polymer Electrode Additives. *J. Power Sources* **2020**, *451*, 227796 DOI: 10.1016/j.jpowsour.2020.227796.
(87) Dong, C.; Liang, J.; He, Y.; Li, C.; Chen, X.; Guo, L.; Tian, F.; Qian, Y.; Xu, L. NiS1.03 Hollow Spheres and Cages as Superhigh Rate Capacity and Stable Anode Materials for Half/Full Sodium-Ion Batteries. *ACS Nano* **2018**, *12* (8), 8277−8287.
(88) Zhao, Y.; Pan, H.; Lou, Y.; Qiu, X.; Zhu, J.; Burda, C. Plasmonic Cu 2-XS Nanocrystals: Optical and Structural Properties of Copper-Deficient Copper(I) Sulfides. *J. Am. Chem. Soc.* **2009**, *131* (12), 4253−4261.
(89) Leidinger, P.; Popescu, R.; Gerthsen, D.; Lünsdorf, H.; Feldmann, C. Nanoscale Copper Sulfide Hollow Spheres with Phase-Engineered Composition: Covellite (CuS), Digenite (Cu1.8S), Chalcocite (Cu2S). *Nanoscale* **2011**, *3* (6), 2544−2551.
(90) Shang, Y.; Li, X.; Huang, S.; Chen, S.; Yang, Z.; Guo, L.; Yang, H. Y. A Selective Reduction Approach to Construct Robust Cu1.81S Truss Structures for High-Performance Sodium Storage. *Matter* **2020**, *2* (2), 428−439.
(91) Yu, H.; Cheng, X.; Xia, M.; Liu, T.; Ye, W.; Zheng, R.; Long, N.; Shui, M.; Shu, J. Pretreated Commercial TiSe2 as an Insertion-Type Potassium Container for Constructing "Rocking-Chair" Type Potassium Ion Batteries. *Energy Storage Mater.* **2019**, *22*, 154−159.
(92) Zhou, J.; Liu, Y.; Zhang, S.; Zhou, T.; Guo, Z. Metal Chalcogenides for Potassium Storage. *InfoMat.* **2020**, *2*, 437−465, DOI: 10.1002/inf2.12101.
(93) Chen, D.; Ji, G.; Ding, B.; Ma, Y.; Qu, B.; Chen, W.; Lee, J. Y. In Situ Nitrogenated Graphene-Few-Layer WS2 Composites for Fast and Reversible Li+ Storage. *Nanoscale* **2013**, *5* (17), 7890−7896.
(94) Lin, W. C.; Yang, Y. C.; Tuan, H. Y. Ternary Chalcogenide Anodes for High-Performance Potassium-Ion Batteries and Hybrid Capacitors via Composition-Mediated Bond Softening and Intermediate Phase. *Energy Storage Mater.* **2022**, *51*, 38−53.
(95) Ma, R.; Wang, M.; Tao, P.; Wang, Y.; Cao, C.; Shan, G.; Yang, S.; Xi, L.; Chung, J. C. Y.; Lu, Z. Fabrication of FeF3 Nanocrystals Dispersed into a Porous Carbon Matrix as a High Performance Cathode Material for Lithium Ion Batteries. *J. Mater. Chem. A Mater.* **2013**, *1* (47), 15060−15067.
(96) Liu, L.; Guo, H.; Zhou, M.; Wei, Q.; Yang, Z.; Shu, H.; Yang, X.; Tan, J.; Yan, Z.; Wang, X. A Comparison among FeF3·3H2O, FeF 3·0.33H2O and FeF3 Cathode Materials for Lithium Ion Batteries: Structural, Electrochemical, and Mechanism Studies. *J. Power Sources* **2013**, *238*, 501−515.
(97) Tang, M.; Zhang, Z.; Wang, Z.; Liu, J.; Yan, H.; Peng, J.; Xu, L.; Guo, S.; Ju, S.; Chen, G. Synthesis of FeF2/Carbon Composite Nanoparticle by One-Pot Solid State Reaction as Cathode Material for Lithium-Ion Battery. *Journal of Materials Research and Technology* **2018**, *7* (1), 73−76.
(98) Ren, Z.; Wen, J.; Liu, W.; Jiang, X.; Dong, Y.; Guo, X.; Zhao, Q.; Ji, G.; Wang, R.; Hu, N.; Qu, B.; Xu, C. Rational Design of Layered SnS2 on Ultralight Graphene Fiber Fabrics as Binder-Free Anodes for Enhanced Practical Capacity of Sodium-Ion Batteries. *Nanomicro Lett.* **2019**, *11* (1), No. 66, DOI: 10.1007/s40820-019-0297-6.
(99) Zhang, F.; Xia, C.; Zhu, J.; Ahmed, B.; Liang, H.; Velusamy, D. B.; Schwingenschlögl, U.; Alshareef, H. N. SnSe2 2D Anodes for Advanced Sodium Ion Batteries. *Adv. Energy Mater.* **2016**, *6* (22), No. 1601188, DOI: 10.1002/aenm.201601188.
(100) Balasingam, S. K.; Lee, J. S.; Jun, Y. Few-Layered MoSe2 Nanosheets as an Advanced Electrode Material for Supercapacitors. *Dalton Transactions* **2015**, *44* (35), 15491−15498.
(101) Fagiolari, L.; Versaci, D.; Di Berardino, F.; Amici, J.; Francia, C.; Bodoardo, S.; Bella, F. An Exploratory Study of MoS2 as Anode Material for Potassium Batteries. *Batteries* **2022**, *8* (11), 242 DOI: 10.3390/batteries8110242.
(102) Qi, H.; Wang, L.; Zuo, T.; Deng, S.; Li, Q.; Liu, Z. H.; Hu, P.; He, X. Hollow Structure VS2@Reduced Graphene Oxide (RGO) Architecture for Enhanced Sodium-Ion Battery Performance. *ChemElectroChem.* **2020**, *7* (1), 78−85.
(103) Mohan, V. V.; Anjana, P. M.; Rakhi, R. B. A Study on the Effect of Phase Conversion of Tungsten Nanostructures on Their Electrochemical Energy Storage Performance. *Mater. Adv.* **2022**, *3* (14), 5900−5910.
(104) Wang, Q.; Guo, C.; Zhu, Y.; He, J.; Wang, H. Reduced Graphene Oxide-Wrapped FeS2 Composite as Anode for High-Performance Sodium-Ion Batteries. *Nanomicro Lett.* **2018**, *10* (2), No. 30, DOI: 10.1007/s40820-017-0183-z.
(105) Li, T.; Dong, H.; Shi, Z.; Yue, H.; Yin, Y.; Li, X.; Zhang, H.; Wu, X.; Li, B.; Yang, S. Composite Nanoarchitectonics with CoS2 Nanoparticles Embedded in Graphene Sheets for an Anode for Lithium-Ion Batteries. *Nanomaterials* **2022**, *12* (4), 724 DOI: 10.3390/nano12040724.
(106) Liu, H.; Li, D.; Liu, H.; Wang, X.; Lu, Y.; Wang, C.; Guo, L. CoSe2 Nanoparticles Anchored on Porous Carbon Network Structure

for Efficient Na-Ion Storage. *J. Colloid Interface Sci.* **2023**, *634*, 864−873.
(107) Xu, X.; Zhou, Y.; You, H.; Min, H.; Wu, X.; Zang, W.; Hao, J.; Feng, Z.; Liu, X.; Yang, H. Engineering Nano-NiS2 Embedded in Graphitized Carbon Skeleton in Hollow Spherical Structure as Stable Anode Material for Reversible Li+ Storage. *Appl. Surf. Sci.* **2022**, *605*, No. 154758, DOI: 10.1016/j.apsusc.2022.154758.
(108) Wen, S.; Zhao, J.; Zhao, Y.; Xu, T.; Xu, J. Reduced Graphene Oxide (RGO) Decorated Sb2S3 Nanorods as Anode Material for Sodium-Ion Batteries. *Chem. Phys. Lett.* **2019**, *716*, 171−176.
(109) Tang, Q.; Song, Y.; Cao, X.; Yang, C.; Wang, D.; Qin, T.; Zhang, W. Interface and Energy Band Manipulation of Bi2O3-Bi2S3 Electrode Enabling Advanced Magnesium-Ion Storage. *Journal of Magnesium and Alloys* **2023**, DOI: 10.1016/j.jma.2023.01.007.
(110) Inoishi, A.; Setoguchi, N.; Hori, H.; Kobayashi, E.; Sakamoto, R.; Sakaebe, H.; Okada, S. FeF3 as Reversible Cathode for All-Solid-State Fluoride Batteries. *Advanced Energy and Sustainability Research* **2022**, *3* (12), No. 2200131, DOI: 10.1002/aesr.202200131.
(111) Lee, C. Y.; Su, Z.; Lee, K.; Tsuchiya, H.; Schmuki, P. Self-Organized Cobalt Fluoride Nanochannel Layers Used as a Pseudocapacitor Material. *Chem. Commun.* **2014**, *50* (53), 7067−7070.
(112) Liu, W.; Hao, J.; Xu, C.; Mou, J.; Dong, L.; Jiang, F.; Kang, Z.; Wu, J.; Jiang, B.; Kang, F. Investigation of Zinc Ion Storage of Transition Metal Oxides, Sulfides, and Borides in Zinc Ion Battery Systems. *Chem. Commun.* **2017**, *53* (51), 6872−6874.
(113) Hoang Huy, V. P.; Ahn, Y. N.; Hur, J. Recent Advances in Transition Metal Dichalcogenide Cathode Materials for Aqueous Rechargeable Multivalent Metal-Ion Batteries. *Nanomaterials* **2021**, *11*, 1517 DOI: 10.3390/nano11061517.
(114) Aurbach, D.; Lu, Z.; Schechter, A.; Gofer, Y.; Gizbar, H.; Turgeman, R.; Cohen, Y.; Moshkovich, M.; Levi, E. Prototype Systems for Rechargeable Magnesium Batteries. *Nature* **2000**, *407*, 724 DOI: 10.1038/35037553.
(115) Zhou, L.; Xiong, F.; Tan, S.; An, Q.; Wang, Z.; Yang, W.; Tao, Z.; Yao, Y.; Chen, J.; Mai, L. Nickel-Iron Bimetallic Diselenides with Enhanced Kinetics for High-Capacity and Long-Life Magnesium Batteries. *Nano Energy* **2018**, *54*, 360−366.
(116) Liu, Y.; He, G.; Jiang, H.; Parkin, I. P.; Shearing, P. R.; Brett, D. J. L. Cathode Design for Aqueous Rechargeable Multivalent Ion Batteries: Challenges and Opportunities. *Advanced Functional Materials* **2021**, *31*, 2010445 DOI: 10.1002/adfm.202010445.
(117) Liang, Y.; Feng, R.; Yang, S.; Ma, H.; Liang, J.; Chen, J. Rechargeable Mg Batteries with Graphene-like MoS2 Cathode and Ultrasmall Mg Nanoparticle Anode. *Adv. Mater.* **2011**, *23* (5), 640−643.
(118) Fan, X.; Gaddam, R. R.; Kumar, N. A.; Zhao, X. S. A Hybrid Mg^{2+}/Li^{+} Battery Based on Interlayer-Expanded MoS2/Graphene Cathode. *Adv. Energy Mater.* **2017**, *7* (19), No. 1700317, DOI: 10.1002/aenm.201700317.
(119) Xu, J.; Wei, Z.; Zhang, S.; Wang, X.; Wang, Y.; He, M.; Huang, K. Hierarchical WSe2 Nanoflower as a Cathode Material for Rechargeable Mg-Ion Batteries. *J. Colloid Interface Sci.* **2021**, *588*, 378−383.
(120) Gu, Y.; Katsura, Y.; Yoshino, T.; Takagi, H.; Taniguchi, K. Rechargeable Magnesium-Ion Battery Based on a TiSe2-Cathode with d-p Orbital Hybridized Electronic Structure. *Sci. Rep* **2015**, *5*, No. 12486, DOI: 10.1038/srep12486.
(121) Pan, W.; Wang, Y.; Zhang, Y.; Kwok, H. Y. H.; Wu, M.; Zhao, X.; Leung, D. Y. C. A Low-Cost and Dendrite-Free Rechargeable Aluminium-Ion Battery with Superior Performance. *J. Mater. Chem. A Mater.* **2019**, *7* (29), 17420−17425.
(122) Li, H.; Ma, L.; Han, C.; Wang, Z.; Liu, Z.; Tang, Z.; Zhi, C. Advanced Rechargeable Zinc-Based Batteries: Recent Progress and Future Perspectives. *Nano Energy* **2019**, *62*, 550−587, DOI: 10.1016/j.nanoen.2019.05.059.
(123) Li, Q.; Bjerrum, N. J. Aluminum as Anode for Energy Storage and Conversion: A Review. *J. Power Sources* **2002**, *110*, 1−10.
(124) Li, Z.; Niu, B.; Liu, J.; Li, J.; Kang, F. Rechargeable Aluminum-Ion Battery Based on MoS2Microsphere Cathode. *ACS Appl. Mater. Interfaces* **2018**, *10* (11), 9451−9459.
(125) Divya, S.; Johnston, J. H.; Nann, T. Molybdenum Dichalcogenide Cathodes for Aluminum-Ion Batteries. *Energy Technology* **2020**, *8* (6), No. 2000038, DOI: 10.1002/ente.202000038.
(126) Xing, W.; Li, X.; Cai, T.; Zhang, Y.; Bai, P.; Xu, J.; Hu, H.; Wu, M.; Xue, Q.; Zhao, Y.; Zhou, J.; Zhuo, S.; Gao, X.; Yan, Z. Layered Double Hydroxides Derived NiCo-Sulfide as a Cathode Material for Aluminum Ion Batteries. *Electrochim. Acta* **2020**, *344*, No. 136174, DOI: 10.1016/j.electacta.2020.136174.
(127) Geng, L.; Scheifers, J. P.; Fu, C.; Zhang, J.; Fokwa, B. P. T.; Guo, J. Titanium Sulfides as Intercalation-Type Cathode Materials for Rechargeable Aluminum Batteries. *ACS Appl. Mater. Interfaces* **2017**, *9* (25), 21251−21257.
(128) Ming, J.; Guo, J.; Xia, C.; Wang, W.; Alshareef, H. N. Zinc-Ion Batteries: Materials, Mechanisms, and Applications. *Materials Science and Engineering R: Reports* **2019**, *135*, 58−84, DOI: 10.1016/j.mser.2018.10.002.
(129) Liang, H.; Cao, Z.; Ming, F.; Zhang, W.; Anjum, D. H.; Cui, Y.; Cavallo, L.; Alshareef, H. N. Aqueous Zinc-Ion Storage in MoS2 by Tuning the Intercalation Energy. *Nano Lett.* **2019**, *19* (5), 3199−3206.
(130) Li, H.; Yang, Q.; Mo, F.; Liang, G.; Liu, Z.; Tang, Z.; Ma, L.; Liu, J.; Shi, Z.; Zhi, C. MoS2 Nanosheets with Expanded Interlayer Spacing for Rechargeable Aqueous Zn-Ion Batteries. *Energy Storage Mater.* **2019**, *19*, 94−101.
(131) Xu, W.; Sun, C.; Zhao, K.; Cheng, X.; Rawal, S.; Xu, Y.; Wang, Y. Defect Engineering Activating (Boosting) Zinc Storage Capacity of MoS2. *Energy Storage Mater.* **2019**, *16*, 527−534.
(132) Yang, Y.; Chuan, X.; Li, J.; Liu, F.; Li, A. Synthesis and Properties of Halloysite Templated Tubular MoS2 as Cathode Material for Rechargeable Aqueous Zn-Ion Batteries. *Int. J. Electrochem Sci.* **2020**, *15*, 6052−6059.
(133) He, P.; Yan, M.; Zhang, G.; Sun, R.; Chen, L.; An, Q.; Mai, L. Layered VS2 Nanosheet-Based Aqueous Zn Ion Battery Cathode. *Adv. Energy Mater.* **2017**, *7* (11), No. 1601920, DOI: 10.1002/aenm.201601920.
(134) Jiao, T.; Yang, Q.; Wu, S.; Wang, Z.; Chen, D.; Shen, D.; Liu, B.; Cheng, J.; Li, H.; Ma, L.; Zhi, C.; Zhang, W. Binder-Free Hierarchical VS2 Electrodes for High-Performance Aqueous Zn Ion Batteries towards Commercial Level Mass Loading. *J. Mater. Chem. A Mater.* **2019**, *7* (27), 16330−16338.
(135) Wu, Z.; Lu, C.; Wang, Y.; Zhang, L.; Jiang, L.; Tian, W.; Cai, C.; Gu, Q.; Sun, Z.; Hu, L. Ultrathin VSe2 Nanosheets with Fast Ion Diffusion and Robust Structural Stability for Rechargeable Zinc-Ion Battery Cathode. *Small* **2020**, *16* (35), No. 2000698, DOI: 10.1002/smll.202000698.
(136) Zhu, Q.; Xiao, Q.; Zhang, B.; Yan, Z.; Liu, X.; Chen, S.; Ren, Z.; Yu, Y. VS4with a Chain Crystal Structure Used as an Intercalation Cathode for Aqueous Zn-Ion Batteries. *J. Mater. Chem. A Mater.* **2020**, *8* (21), 10761−10766.
(137) Hoang Huy, V. P.; Ahn, Y. N.; Hur, J. Recent Advances in Transition Metal Dichalcogenide Cathode Materials for Aqueous Rechargeable Multivalent Metal-Ion Batteries. *Nanomaterials* **2021**, *11*, 1517. DOI: 10.3390/nano11061517.
(138) Li, B.; Li, Z.; Chen, H.; Zhang, X.; Wu, S.; Xu, H.; Yao, Y.; Li, Y.; Li, X.; Hu, Z.; Laine, R. M.; Zou, J.; Zhang, K. Li^{+} Additive Accelerated Structural Transformation of MoS2 Cathodes for Performance-Enhancing Rechargeable Mg2+ Batteries. *Mater. Today Energy* **2022**, *27*, No. 101047, DOI: 10.1016/j.mtener.2022.101047.
(139) Hao, Q.; Cui, G.; Zhao, Y.; Bakenov, Z. Flower-like MoSe2/MoO2 Composite with High Capacity and Long-Term Stability for Lithium-Ion Battery. *Nanomaterials* **2019**, *9* (9), 1256 DOI: 10.3390/nano9091256.
(140) Gu, Y.; Katsura, Y.; Yoshino, T.; Takagi, H.; Taniguchi, K. Rechargeable Magnesium-Ion Battery Based on a TiSe2-Cathode with

https://doi.org/10.1021/acsomega.3c08809
ACS Omega 2024, 9, 7357−7374

d-p Orbital Hybridized Electronic Structure. *Sci. Rep* **2015**, *5*, No. 12486, DOI: 10.1038/srep12486.
(141) Alahmadi, M.; Farrag, M.; El-Dok, E.; Moselhy, M. A.; Sheha, E. Evaluation of the Performance of VSe2 Cathode in Halogen-Free Electrolyte for Magnesium Battery Applications. *Mater. Lett.* **2023**, *341*, No. 134300, DOI: 10.1016/j.matlet.2023.134300.
(142) Ko, J.; Kang, S. H.; Cheong, H. W.; Yoon, Y. S. Recent Progress in Cathode Materials for Thermal Batteries. *Journal of the Korean Ceramic Society* **2019**, *56* (3), 233−255.

https://doi.org/10.1021/acsomega.3c08809
ACS Omega 2024, 9, 7357−7374